GOLD SUPPORTED ON TUNGSTATED ZIRCONIA: SYNTHESIS, CHARACTERIZATION and IN SITU FT-IR INVESTIGATION of NO_x+C_3H_6 SURFACE REACTIONS

A THESIS

SUBMITTED TO THE DEPARTMENT OF CHEMISTRY AND

THE GRADUATE SCHOOL OF ENGINEERING AND SCIENCES OF

BILKENT UNIVERSITY

IN PARTIAL FULFILLMENT OF THE REQUIREMENTS

FOR THE DEGREE

OF

MASTER OF SCIENCE

By

SERDAR MAMETSHERIPOV

MAY 2012

I certify that I have read this thesis and in my opinion it is fully adequate, in scope and in quality, as a thesis of the degree of Master of Science

_____

Assoc. Prof. Dr. Margarita Kantcheva (Supervisor)

I certify that I have read this thesis and in my opinion it is fully adequate, in scope and in quality, as a thesis of the degree of Master of Science

_____

Prof. Dr. Şefik Süzer

I certify that I have read this thesis and in my opinion it is fully adequate, in scope and in quality, as a thesis of the degree of Master of Science

_____

Prof. Dr. Gürkan Karakaş

I certify that I have read this thesis and in my opinion it is fully adequate, in scope and in quality, as a thesis of the degree of Master of Science

_____

Prof. Dr. Ömer Dağ

I certify that I have read this thesis and in my opinion it is fully adequate, in scope and in quality, as a thesis of the degree of Master of Science

_____

Assist. Prof. Dr. Emrah Özensoy

Approved for the Institute of Engineering and Sciences

_____

Prof. Dr. Levent Onural

Director of Institute of Engineering and Sciences

ABSTRACT

GOLD SUPPORTED ON TUNGSTATED ZIRCONIA: SYNTHESIS, CHARACTERIZATION and IN SITU FT-IR INVESTIGATION of NO_x+C_3H_6 SURFACE REACTIONS

Serdar Mametsheripov

M.Sc in Chemistry

Supervisor: Assoc. Prof. Dr. Margarita Kantcheva

May 2012

The potential of gold supported on tungstated zirconia as a catalyst for selective catalytic reduction of NO_x with propene (C_3H_6-SCR) was investigated by in situ FT-IR spectroscopy. Samples of tungstated zirconia were prepared by both impregnation and coprecipitation methods using ammonium metatungstate (AMT) as a precursor. Gold was deposited on the supports via cationic adsorption from aqueous solution of $[Au(en)_2]Cl_3$ complex (en = ethylenediamine). The samples were characterized by XRD, XPS, BET, DR-UV-vis, ICP-MS and FT-IR spectroscopy of adsorbed CO. The results show that the samples consist of tetragonal zirconia crystallites hosting uniform layer of polytungstate species. The gold particles occupy preferentially the WO_x-free zirconia surface and the dispersion of gold depends on the amount of coodinatively unsaturated (cus) Zr^{4+} ions. The modification of zirconia by tungsten facilitates the gold uptake but at the same time causes decrease in the concentration of (cus) Zr^{4+} ions thus lowering the despersion of gold clusters.

The interaction of gold supported on WO_x-free (Au/ZrO_2) and WO_x-modified zirconia samples (Au/xWZ-I, where "I" denotes the incorporation of WO_3 by impregnation and x = 5, 12, and 20 wt % of WO_3) with NO+O_2 gas mixture shows that the W-containing samples promote the formation of NO_2 at room temperature. The FT-IR spectra obtained at room

temperature during the contact of CO with gold samples containing pre-adsorbed NO_x species reveal the formation of isocyanates (NCO) coordinated to gold sites. The generation of Au–NCO species in the ad-NO_x+CO reaction is confirmed by using ^{13}CO and treatment of the adsorbed isocyanates with water vapor. The gold isocyanates display high thermal stability. However, they react readily with NO_2 at room temperature. This finding suggests that gold supported on tungstated zirconia could be of interest as a low-temperature catalyst for CO-SCR of NO_x.

The FT-IR spectra recorded during the contact of C_3H_6 and O_2 gas mixture with Au/ZrO_2 and Au/xWZ-I samples lead to the conclusion that the WO_x-free sample catalyzes the complete oxidation of propene. The Au-promoted tungstated samples, which contain redox (W=O groups) and Brønsted acid sites, favor the partial oxidation of the hydrocarbon.

The results of a detailed mechanistic investigation show that the activation of propene in the presence of NO_x species adsorbed on Au/xWZ-I samples takes place at room temperature producing surface isopropoxides. The interaction of the latter species with the surface nitrate complexes leads to the formation of nitroacetone [$CH_3C(O)CH_2NO_2$]. It is proposed that at higher temperatures (e.g. 150^oC) the nitroacetone coordinated to gold particles transforms through an internal redox process producing surface acetates and Au–NCO species. The isocyanates react with the NO_3^-/NO_2 surface complex formed by oxidation of NO yielding molecular nitrogen, N_2O and CO_x as reaction products. The gold-free samples do not cause the formation of NCO species under the same experimental conditions. This experimental fact suggests that the Au particles play fundamental role in the formation of the NCO species. The amount of Au-NCO species produced is the highest on ZrO_2-based catalyst containing 1.8 wt % of gold and 12 wt % of WO_3 (Au/12WZ-I sample). This material combines better gold dispersion with sufficient amount of Brønsted acid sites necessary for the activation of propene to hydrocarbon oxygenates leading to the formation of nitroacetone. Based on the catalytic activity measurements, it is concluded that among the materials studied, the Au/12WZ-I catalyst could be promising in the C_3H_6-SCR of NO_x.

V

ÖZET

TUNGSTENLENMİŞ ZİRKONİYA DESTEKLİ ALTIN: SENTEZ, NİTELEME ve NO$_x$+C$_3$H$_6$ YÜZEY TEPKİMELERİN YERİNDE FT-IR İLE İNCELENMESİ

Serdar Mametsheripov

Kimya Bölümü Yüksek Lisans

Danışman: Doç. Dr. Margarita Kantcheva

Mayıs 2012

Tungstenlenmiş zirkoniya destekli altının azot oksitlerin (NO$_x$) propenle seçici katalitik indirgenmesini (SKİ) katalizleme potansiyeli yerinde FT-IR spektroskopisiyle incelenmiştir. Tungstenlenmiş zirkoniya numuneleri hem doyurulma hem ortak çöktürme yöntemleriyle amonyum metatungstat (AMT) öncülünden sentezlendi. Altın, destek malzemeleri üzerine (Au(en)$_2$]Cl$_3$ kompleksin (en=etilendiamin) sulu çözeltisinden katyonik adsorpsiyon yöntemiyle depolandı. Numunelerin yapısal ve yüzey özellikleri XRD, XPS, BET, DR-UV-Vis, ICP-MS ve FTIR spektroskopisi yöntemleriyle incelendi. Alınan sonuçlara göre, numuneler politungstat türlerin tek katman tabakasını barındıran tetragonal zirkoniya kristalitlerinden oluşmaktadır. Altın parçacıkları, tercihen WO$_x$-içermeyen zirkoniya yüzeyinde yerleşmekte ve altının dağılımı doymamış koordinasyona sahip Zr^{4+} iyonların miktarına bağlıdır. Zirkoniyanın tungstenle değiştirilmesi altının depolanmasını kolaylaştırmakta ancak aynı zamanda doymamış koordinasyona sahip Zr^{4+} iyonların miktarını azaltarak altın kümelerinin dağılımını azaltmaktadır.

WO$_x$-içermeyen (Au/ZrO$_2$) ve WO$_x$-içeren zirkoniya destekli altın (Au/xWZ-I, "I" doyurulma yöntemiyle WO$_3$'nın eklenmesini ve x = 5,12, ve 20 WO$_3$'nın kütlesel yüzdesini simgelemekte) numunelerinin NO+O$_2$ gaz karışımıyla olan etkileşimi göstermektedirki, WO$_x$-içeren numuneler oda sıcaklığında NO$_2$ oluşumunu sağlamaktadır. Oda sıcaklığında CO'nun

önceden adsorplanmış NO_x türlerini içeren altın numuneleri ile teması sonrası elde edilen FT-IR sonuçları altına koordine olmuş izosiyanür (NCO) oluşumunu açığa çıkarmaktadır. Ads-NO_x+CO tepkimesi sonucu Au−NCO türlerinin oluşumu ^{13}CO kullanarak ve adsorplanmış izosiyanürlerin su buharı ile etkileşimini kullanarak ile teyit edilmiştir. Altın izosiyanürleri yüksek ısıl kararlılık göstermekte, ancak NO_2 ile oda sıcaklığında kolayca tepkimeye girmektedir. Bu bulgular, tungstenlenmiş zirkoniya destekli altının NO_x'ın CO-SKİ'si için düşük-sıcaklık katalizatörü olması açısından umut verici olduğuna işaret etmektedir.

C_3H_6 ve O_2 gaz karışımının Au/ZrO_2 ve Au/xWZ-I numuneleriyle teması sırasında kaydedilen FT-IR verileri Au/ZrO_2 numunesinin propenin derin yükseltgenmesini katalizlediği sonucuna varmamızı sağlamaktadır. Yükselgeme-indirgeme (W=O grupları) ve Brønsted asit bölgeleri içeren altın depolanmış tungstenlenmiş numuneler hidrokarbonun kısmi yükseltgenmesini sağlamaktadırlar.

Detaylı bir mekanistik inceleme sonucuna göre, Au/xWZ-I numunelerine adsorplanmış NO_x türleri ortamında, propen, oda sıcaklığında izopropoksite dönüşmesi suretiyle aktif hale gelmektedir. İzopropoksidin yüzey nitrat kompleksleriyle etkileşimi nitroaseton [$CH_3C(O)CH_2NO_2$] oluşumuna neden olmaktadır. Daha yüksek sıcaklıklarda (150^oC) altın parçacıklarına koordine olmuş nitroasetonun içsel bir yükseltgenme-indirgenme süreciyle yüzey asetat ve Au−NCO türlerine dönüştüğü önerilmektedir. İzosiyanürler NO yükseltgenmesi sonucu oluşan yüzey NO_3^-/NO_2 kompleksleriyle tepkimeye girerek moleküler azot, N_2O ve CO_x'u oluşturur. Aynı deneysel koşullar altında altınsız numuneler NCO türlerin oluşumuna neden olmamaktadır. Bu deneysel gerçek, Au parçacıklarının NCO türlerin oluşumunda önemli bir rol oynadığını göstermektedir. Au−NCO türlerinin miktarının en çok olduğu durum kütlece %1.8 altın ve %12 WO_3 (Au/12WZ-I numunesi) içeren ZrO_2-bazlı katalizatör yüzeyindedir. Bu malzeme iki önemli özelliğe sahip. Birincisi, yüzeyinde altın parçacıkların çok iyi bir şekilde dağılmış olması, ikincisi ise yüzeyinde yeteri miktarda Brønsted asit bölgelerini bulundurmasıdır (propenin aktif hale gelmesi için gerekli). Katalitik etkinlik ölçümlerine dayanılarak, incelenilen maddeler arasında Au/12WZ-I katalizatörünün NO_x'ın C_3H_6-SKİ'si için gelecek vaadettiği sonucuna varılmıştır.

Anahtar Kelimeler: Yerinde FT-IR; Tungstenlenmiş zirkoniya destekli altın; NO_x'ın propenle seçici katalitik indirgenmesi; Mekanizma, Reaktif araürünler.

ACKNOWLEDGEMENT

TABLE OF CONTENTS

LIST OF TABLES

LIST OF FIGURES

XIII

LIST OF ABBREVIATIONS

BE: binding energy, *page 13*

cus: coordinatively unsaturated site(s), *page 27*

DP: deposition precipitation, *page 15*

en: ethylenediamine, *page III*

HC: hydrocarbon, *page 1*

IEP: isoelectric point, *page 10*

LMCT: ligand to metal charge transfer, *page 21*

RT: room temperature, *page 14*

SCR: selective catalytic reduction, *page 1*

TWC: three way catalyst, *page 1*

WHSV: weight hourly space velocity, *page 15*

WGS: water gas shift reaction, *page 12*

Notation and composition of the investigated Au-containing samples

Sample Notation	Au* wt.%	WO_3 wt %	Method of synthesis of tungstated zirconia
Au/ZrO₂	1.43	-	-
Au/5WZ-I	1.27	5.0	Impregnation of hydrated zirconia with aqueous solution of ammonium metatungstate.
Au/12WZ-I	1.83	11.8	Impregnation of hydrated zirconia with aqueous solution of ammonium metatungstate
Au/20WZ-I	2.06	19.4	Impregnation of hydrated zirconia with aqueous solution of ammonium metatungstate.
Au/18WZ-CP	2.27	18.0	Coprecipitation of aqueous solutions of $ZrOCl_2$ and ammonium metatungstate with ammonia at pH=9.

*For all samples gold was introduced by cationic adsorption using aqueous solution of $[Au(en)_2]Cl_3$

1. INTRODUCTION

1.1 Environment pollution and exhaust emissions

It is now widely believed that global warming is caused by deforestation and burning of the fossil fuels [1]. These fossil fuels when burned produce green house gases such as CO_2, CH_4 etc [2]. Greenhouse gases and other air pollutants mainly originate from stationary (e.g. industrial power plants etc) and mobile (cars, trucks etc) sources. Main pollutants in the vehicle exhaust gases are unburned hydrocarbons (HC), CO and NO_x (NO and NO_2). To prevent the pollution, rules and regulations which control and limit the amounts of pollutants have been set. In Europe for passenger cars which use diesel Euro 5, NO_x emission standard was 0.180 g/km by 2009 [3]. Various technologies have been developed and applied to meet these standards. Perhaps the most known among them are the Three Way Catalytic (TWC) converters for the internal combustion gasoline engines. This system consists of catalysts which promote oxidation of CO, HC and reduction of NO_x to N_2 simultaneously [4]. Even if this system proved to be useful for gasoline engines, it can not supply efficient control of NO_x emissions for diesel and lean-burn engines (they operate at air to fuel ratio of 17-26) [4]. To overcome this problem various catalytic techniques have been proposed.

1.2 Catalytic techniques for NO_x post-combustion abatement under lean conditions

There are three main catalytic technologies used for removal of NO_x from the exhaust gases of lean burn and diesel vehicles [5-8]. These are 1) NO_x storage; 2) urea-selective catalytic reduction (urea-SCR) and 3) hydrocarbon-selective reduction (HC-SCR). All of these techniques mentioned above have important drawbacks.

1.2.1 NO_x storage and Reduction

This process consists of two steps [5-9]: 1) NO_x storage over the Ba sites (which are in the form of $BaCO_3$ due to presence of CO_2 in the exhaust gas phase). This step occurs during

the normal operation of the engine under lean conditions. 2) Regeneration and cleaning up of the catalyst surface via desorption and reduction of NO_x with the help of a noble metal. Generally a NO_x storage catalyst has two noble metal components Pt or Pd, that will help oxidation of NO, CO and hydrocarbons (HC) under lean operating conditions and Rh for the purpose of reducing the NO_x by CO under reach regeneration conditions [7-9]. The NO_x storage technology is commercialized in Japan.

Major disadvantages of a NO_x storage system for diesel engines can be listed as fuel over-consumption during the regeneration phase (to supply enough amount of reductant engine control systems are mounted and this leads to over-consumption), methane emission, sulfur sensitivity, difference in performance of NO_x removal system at low and high temperatures, thermal deactivation of the catalyst, high cost of the system.

At the onset of the catalyst regeneration step significant amount of reductants (CO, H_2, hydrocarbons including methane) are produced in the engine. All of the reductants but methane are consumed by adsorbed NO_x. Methane (a greenhouse gas) leaves the NO_x storage system intact and contributes to the overall hydrocarbon emission from the vehicle exhaust. This extra content of HC challenges the emission standard set by Diesel Euro standards [9]. To overcome this problem sometimes cars are designed in such a way that they have special injector in the exhaust line that provides the necessary reductants directly from the fuel tank and prevents the release of methane. This application obviously results in higher fuel consumption [9].

The NO_x storage system cannot be used for fuels with high concentration of sulfur [5-9]. Nowadays it is used in Japan where vehicle are loaded with low sulfur content fuels [6]. Gasoline used in US and Europe has high sulfur content and during engine operation acidic sulfur oxides form and they adsorb stronger than NO_x on the catalyst surface in this way poisoning the catalyst (especially alkaline earth metal component). Using low-content sulfur (<10 ppm) fuel is not an option because lubricant also contains sufficient amount of sulfur to cause the deactivation of the NO_x storage catalyst. The sulfur concentration in lubricant cannot be reduced because it determines the lubrication property [9].

To be suitable for application in light duty diesel vehicles the activity window of the NO_x storage catalyst must be in the range of 150-350°C [10] which is much lower when compared to gasoline engine. Because at low temperatures oxidation of NO to NO_2 becomes the controlling factor, separation of NO_x storage property from the NO oxidation property is necessary [10]. At low temperature and rich conditions the overall activity of the catalyst is determined by decomposition rate of stored nitrates and reduction rate of NO_x. Temperatures

as high as 600^0C can be reached in heavy duty diesel systems. At high temperatures thermodynamic stability of stored nitrates may be an important problem. This can result in insufficient adsorption of NO_x and NO_x slip may occur during the lean periods [10].

The NO_x storage catalyst can get thermally deactivated through the sintering of barium species and formation of barium aluminates [5-9].

High content of precious metals (Pt and Rh) in the catalyst makes the NO_x storage system application costly. So far rhodium price has been incessantly increasing and in 2006 price of it reached more than three times the price in previous year [9]. By March 2012 its price was about 1500$ per ounce (www.kitco.com) and of Pt was 1600$ per troy ounce (money.cnn.com).

1.2.2 Urea- Selective Catalytic Reduction

The urea-SCR has been used as a NO_x removal technology for heavy-duty trucks and buses in Europe since 2005 [11]. However it has been used in industrial stationary applications since 1970s and has evolved a lot since then [12]. This system exploits interaction of ammonia with NO_x over the catalyst (vanadia supported on titania with WO_3 and MoO_3 as promoters). Aqueous urea solution is used as a source of ammonia because ammonia is toxic and corrosive and a gas difficult to handle [11]. The urea-SCR system occupies a lot of volume onboard because it consists of large number of parts [9]:

- Urea injector and a control unit for adjustment of quantity injected.
- Additional tank to store urea solution.
- A mixer at the catalyst inlet to provide a uniform ammonia concentration in exhaust gas.
- A catalyst to facilitate hydrolysis of urea to ammonia.
- SCR catalyst for NO_x reduction.
- A clean-up catalyst for maintaining proper amount of ammonia (10 ppm) released from exhaust.
- NO_x sensor to control the amount of ammonia injected and for diagnosis of the urea-SCR system

The urea-SCR is most efficient in the temperature range $250 - 400^0C$ [9,11,12]. Before the operation the SCR and the urea catalysts must be pre-heated. NO_x conversion is dependent on NO to NO_2 ratio and optimum conversion is achieved when this ratio is 1. Thus a NO

oxidation catalyst is needed to be installed upstream of the system [9]. Installation of the urea-SCR system into the passenger cars is not feasible due to unavailability of enough space [9]. Deficiency in infrastructure in terms of availability of urea along with fuel is yet another setback [5, 9]. Moreover urea solution has freezing point of -11^0C making application of this system in cold countries impossible [9]. In high oxidative conditions sulfur from the diesel fuel is oxidized to sulfur dioxide which can react with ammonia to produce ammonium sulfate. Build up of this compound on catalyst surface can cause irreversible deactivation [13]. Besides this at low temperatures $(100-200^0$C) ammonia and nitrogen dioxide together can form ammonium nitrate, the explosive which can also temporarily deactivate the catalyst via accumulation inside the pores of the catalyst in solid or liquid form [12]. Finally it should be noted that an effective urea injection system is not available so far and this complicates the control of ammonia slip and secondary emissions [5-9].

1.2.3 Hydrocarbon (HC) - Selective Catalytic Reduction

In HC-SCR system either hydrocarbon that already exists in the exhaust is used (passive control) or it is added as a fuel upstream of catalytic converter (active control) to reduce NO_x [5,7]. In 1990 two groups (Held et al. [14] and Iwamoto et al. [15]) independently discovered that Cu/ZSM-5 is active for SCR of NO with alkanes and alkenes in the presence of oxygen. Since then much work was done on this subject and a lot of catalysts both zeolitic and non-zeolitic have been proposed [7,8,16,17]. However it was found out that zeolite-based catalysts did not have hydrothermal stability making them inapplicable to real exhaust conditions [7,8]. Thus focus was shifted to metal oxide catalysts. In literature there are several review papers dealing with oxide based HC-SCR [8,16,17]. Metals Mn, Fe, Co, Ni, Cu, Sn, Ga, In and Ag (promoters) when combined with Al_2O_3, TiO_2, ZrO_2, MgO are catalytically active in the selective reduction of NO_x with hydrocarbons. Silica is not active itself but can be used as a support. Under lean conditions the promoter metals tend to exist in oxidized state [17]. The performance of these oxide based HC-SCR catalysts strongly depends on functionality of the hydrocarbon (alkane, alkene, alcohol) and the carbon number. The higher the carbon number in the reducer, the lower the activity temperature range [8,16,17]. Nevertheless C_2-C_3 alkenes and alkanes have been extensively tested because these hydrocarbons are present in the automobile exhaust gas mixture [17].

In HC-SCR of NO_x, the extent of reduction of NO_x is determined by type of the metal and the hydrocarbon used. Among the noble metals, platinum is the most active and selective

metal [8,17]. Depending on the type of the hydrocarbon present Pt can exist in either oxidized or reduced state during the selective oxidation of NO in excess oxygen atmosphere [17]. In the presence of strongly adsorbing hydrocarbons like propene and lighter alkanes, the excess oxygen cannot oxidize the platinum because it is covered with hydrocarbonaceous residues. Whereas methane and propane cannot prevent the oxidation of platinum. The reduction of NO takes place on the surface of reduced Pt covered with hydrocarbonaceous residues [17]. Despite the fact that non-zeolitic catalysts are hydrothermally stable they cannot be used at low temperatures because they generally show activity at high temperatures (above 300^0C) [7,8,16,17]. Platinum supported on alumina however is an exception with the maximum activity attained at 250^0C. Unfortunately the activity temperature range is narrow and has low N_2 selectivity producing significant amount of byproduct N_2O at low temperatures [7,8,17]. Investigations with $Zr_6Nb_2O_{17}$ solid solution have shown that maximum activity is reached already at 220^0C in the selective catalytic reduction of NO_x with propene [18].

Lately, silver supported on alumina in low loadings attracted much attention as a catalyst for HC-SCR of NO_x [5,8,19]. In the presence of various hydrocarbons as reductants these catalysts are active and selectively promote the formation of N_2. However they have the same disadvantages as other oxide based catalysts: narrow temperature window and low activity in low temperature region (150-350^0C, the diesel exhaust conditions) [5-8,10,19]. One way of overcoming this problem can be adding of H_2 to the feed [5,8,19]. The activity of catalysts improves a great deal especially when a reactive reductant such as octane is used. In the absence of hydrogen activity begins to increase at 350^0C and becomes maximum at approximately 500^0C before going downhill again. However when only 0.72 % H_2 is added to the feed reaction begins at 100^0C and conversion has a peak value already at 200^0C. The effect of hydrogen on the activity of Ag/Al_2O_3 catalysts is especially interesting because it is believed that it offers a promising way for continuous reduction of NO_x emissions under lean conditions using diesel added prior to the catalyst (active NO_x control) [5]. In order to make this strategy competitive, further development is needed regarding on-board production of H_2. In addition, the extensive sintering of supported silver and sulfur poisoning may represent an important drawback for practical application [7].

Literature review reveals that gold supported on ZnO, MgO, TiO_2, ZrO_2, Al_2O_3, Fe_2O_3 [20,21] is fairly active in selective reduction of NO_x to N_2 with propene in the presence of oxygen in the temperature range 200-500^0C. The activity temperature is dictated by the type of the support used. Au/ZnO shows activity at 250^0C with the NO to N_2 conversion of 32-49

% [20,21]. At 250^0C nanosized gold supported on zirconia can achieve 32 % of NO conversion in the reduction with propene in excess oxygen atmosphere [20]. Gold supported on alumina is even better, resulting in 80 % NO to N_2 conversion, however at 450^0C [20,21]. On the other hand Au on TiO_2 is active at 350^0C [20]. A mechanism in which NO is first oxidized to NO_2 which is then reduced to molecular nitrogen by an activated propene species have been proposed for this catalytic systems [20,21]. According to the kinetic data [20-23] collected for reduction of NO catalyzed by gold supported on alumina and titania, the oxidation of NO to NO_2 is rate-determining step. Mechanical mixtures with Mn_2O_3 or CeO_2 (to boost the oxidation of NO) increase the catalytic activity by pulling down the temperature of maximum conversion of NO to N_2 to $225-300^0C$ range [20,22,23]. This effect is attributed to bifunctional mechanism in these systems [24,25]. In this mechanism NO is oxidized with molecular oxygen over Mn_2O_3 to form NO_2 in gas phase, which then reacts with propene adsorbed on the surface of gold particles [20,22]. It should be noted that the gold deposited on solely Mn_2O_3 or CeO_2 is not good for SCR of NO with propene because it completely oxidizes the hydrocarbon to CO_2 [22,26]. This is also supported by the fact that gold dispersed on easily reducible supports is not active for partial oxidation of propene [27]. However, when gold is supported on less reducible oxides like V_2O_5 and MoO_3 , the propene is partially oxidized to propanal, acetone, ethanal and acetic acid [27]. It is known that V_2O_5 and MoO_3 supported on silica have Brønsted acid sites on their surfaces [28]. FT-IR spectroscopic research has revealed that the activation process of propene over the catalysts which have Brønsted acid sites consists of formation of isopropoxide species on the catalyst surface and then with the increase in temperature further oxidation to acetone and acetate species takes place [18,29,30]. In SCR of NO_x with propene, these products of partial oxidation are key intermediates and they form nitrogen containing organic compounds which then react with $NO+O_2/NO_2$ at high temperatures to produce N_2. Brønsted acids like WO_3/ZrO_2 and $Zr_6Nb_2O_{17}$ can catalyze the oxidation of NO by O_2 already at room temperature and W^{6+} and Nb^{5+} ions are responsible for this [18,31]. It can be concluded that oxide systems which have strong Brønsted acid sites like WO_3 supported on zirconia can provide both oxidation of NO and activation of propene. The bifunctional property of these oxides makes them potential component of gold containing catalysts for the low temperature $DeNO_x$. It is proposed [32] that dispersed gold can promote the activity of the support for the oxidation of NO to NO_2 in the wide temperature range. Moreover when compared with the amphoteric zirconia the acidic tungstated zirconia should show more resistance to SO_2 poisoning which could be one of the reasons for deactivation of catalysts.

1.3 Mechanism of HC-SCR of NO_x on non-zeolitic oxide-based catalysts

In order to be able to properly design and apply the SCR technology it is important to understand the chemistry of this process in terms of mechanism. In the review made by Burch et al. [8,17] for non-zeolitic oxide based catalysts it is reported that over oxide-supported platinum group metals NO_x reduction consists of two steps. First, NO is dissociatively adsorbed on reduced noble metal and second, two adsorbed nitrogen atoms recombine to form molecular nitrogen [33]. Hydrocarbon maintains the removal of atomic oxygen (coming from NO dissociation) and dissociation of O_2 to regenerate the reduced metal surface [33]. Even if for noble metal catalysts the above explained mechanism was proven, it was also shown that mechanisms observed in the case of metal-free oxide catalysts may also operate for metal-promoted catalysts [8,17 and references therein].

For noble metal-free oxide based catalysts two different $DeNO_x$ mechanisms have been proposed regardless of the nature of the catalyst and the reductant used [8,17]. In the first mechanism, the so called NO reaction pathway [8,17], gaseous or adsorbed NO_x species interacts with hydrocarbons (HC) [34-53] forming organic nitro compounds ($R-NO_2$) as intermediates [18,34-51]. These intermediates may produce molecular nitrogen directly [35-37] or decompose into other intermediates like isocyanates [18,34,36,38-47], ammonia [40,41,44,45,47], oximes [43], nitriles [46,47], hydrocarbon oxygenates and adsorbed NO [50-53]. It was suggested by Thomas et al. [50,51] that the hydrocarbon oxygenates reduce the adsorbed oxygen produced by decomposition of NO to N_2 as a result regenerating the corresponding catalytic sites. Kantcheva and Cayirtepe [52] detected the formation of methyl nitrite (which originates from nitromethane intermediate) as a result of interaction of methane with NO_x species adsorbed on the surface of Pd-promoted tungstated zirconia. The organic nitrite decomposed to adsorbed NO and formates which reacted further to molecular nitrogen. The same pathway is suggested in the case of CH_4-SCR of NO over $Pd/Zr_2Nb_6O_{17}$ catalyst [53]. The DRIFT studies carried on $Au/\gamma-Al_2O_3$ [54] revealed that the selective reduction of NO with propene consisted of oxidation of NO to NO_2 and interaction of NO_2 or its adsorbed species (nitrates or nitrites) with activated propene to form $R-NO_x$ adsorbed on the support. Although the latter surface compound was not detected, it is thought that it experienced an internal rearrangement and decomposition to NCO and CN species which further reacted with $NO+O_2$ or NO_2 to form nitrogen. The observation that model nitroorganic compounds

produced similar products as a result of decomposition during the SCR reactions supports the importance of nitroorganic compounds as intermediates [35,40-42,45-49,52].

The second so called hydrocarbon pathway [8,17] takes into account the presence of two possible oxidants, O_2 and NO_x, in the reaction gas mixture or strongly adsorbed NO_x species (nitrites and/or nitrates) on the catalyst surface, which can activate the HC producing oxygenates [55-59]. These compounds reduce the surface NO_x species to molecular nitrogen. Increase in $DeNO_x$ activity when oxygenates are used as reductants supports this mechanism proposal [34,42,60-66].

Scheme 1 (adopted from references [8,17]) summarizes all of the proposed mechanisms for SCR of NO_x on oxide based catalysts. It can be concluded that there is no general agreement about the actual mechanism [8,16,17].
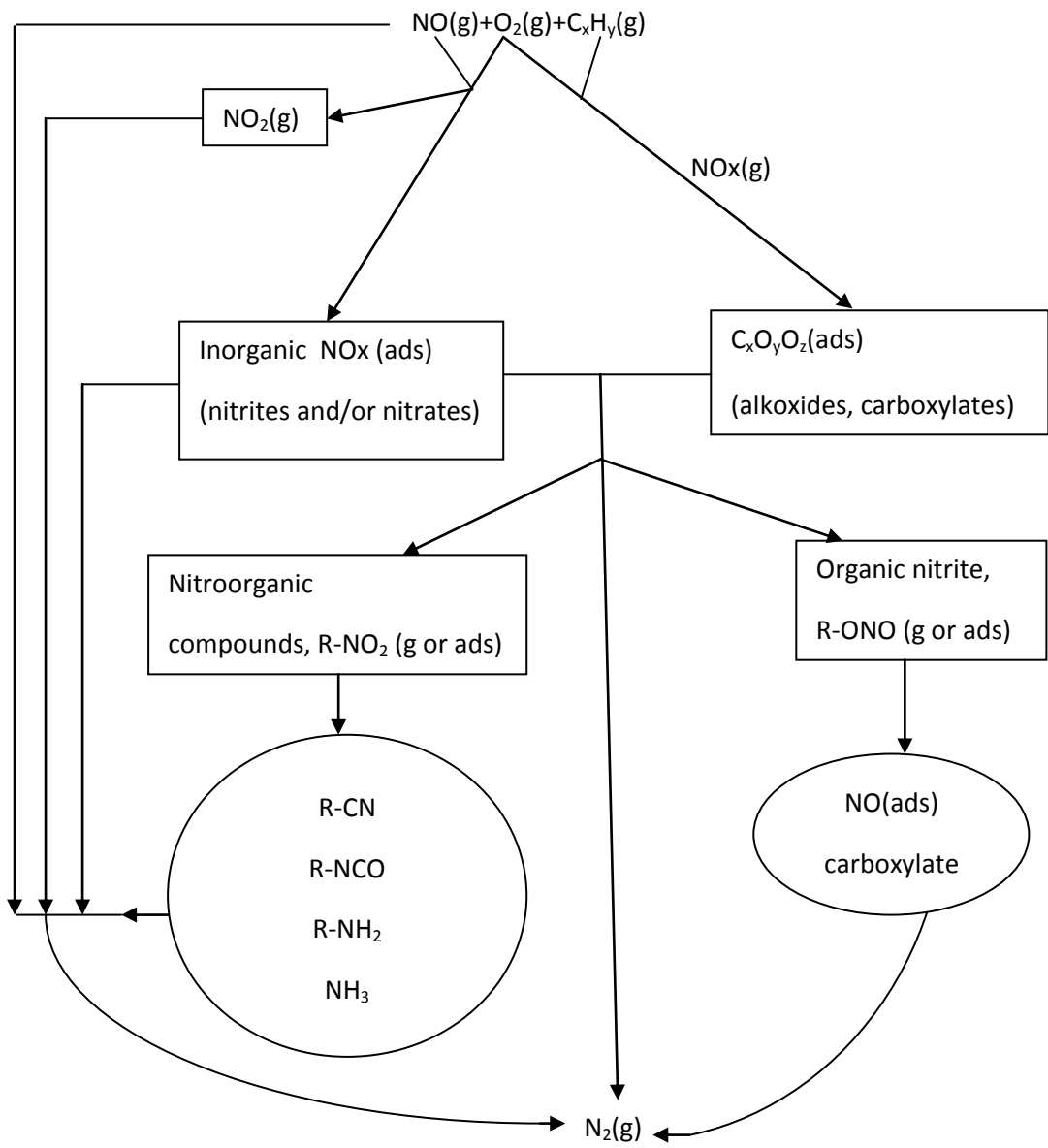
Scheme 1. Reaction scheme of the HC-SCR of NO over oxide catalysts

1.4 Aim of Study

The objectives of the investigation are to develop an efficient synthetic approach for the deposition of nanosized gold particles on WO_x-modified zirconia and to evaluate the potential of the gold-promoted solid acids as catalysts for the low-temperature C_3H_6-SCR of NO_x by using in situ FT-IR spectroscopy. To the best of our knowledge, the performance of gold supported on WO_x-modified zirconia in the SCR of NO_x with hydrocarbons has not been investigated to date.

Before the use of new catalysts in the C_3H_6-SCR of NO_x, it is important to know whether all reagents, such as NO, reductant and O_2, are chemisorbed on the catalyst surface and which kinds of intermediates are formed. For that purpose the adsorption and co-

adsorption of the reagents is investigated by means of in situ FT-IR spectroscopy followed by their interaction at various temperatures. Other techniques, including UV-Visible spectroscopy, XRD, XPS, BET are used to complete the characterization of the catalyst structures. The localization of the WO_x and gold species (including the oxidation state of the latter) on the surface of zirconia is investigated by FT-IR spectroscopy of adsorbed CO. The amount of deposited gold and tungsten is determined by chemical analysis. The activity of selected samples is tested in the C_3H_6-SCR of NO.

2. EXPERIMENTAL

2.1. Sample preparation

Two different procedures were used for preparation of hydrated zirconia. According to procedure 1, hydrated zirconia (denoted as HZ-1) was prepared by hydrolysis of 0.3 M solution of zirconyl chloride (ZrOCl$_2$·H$_2$O, Aldrich) with concentrated (25%) ammonia solution at pH 9. The slurry of the precipitated material was kept for aging at room temperature for 12 h. Then the product was separated by vacuum filtration, redispersed in deionized water, washed thoroughly to remove the chloride ions and dried at 100^{0}C. The crystallographic structure of the material obtained after calcination at 600^{0}C was predominantly monoclinic zirconia. Tungstated zirconia was synthesized by coprecipitation [67] with nominal content of 18 wt % WO$_3$ and by impregnation of HZ-1 with aqueous solution of ammonium metatungstate (AMT, Fluka) using the method proposed by Martinez et al. [68]. This procedure consisted of impregnation of HZ-1 with aqueous solution (3 mL/g hydrated zirconia) containing the required amount of AMT to obtain WO$_3$ loadings corresponding to 5, 12 and 20 wt%. The final calcination temperature of all tungstated zirconias was 600^{0}C. Gold was deposited by cation adsorption for 2 h from aqueous solution of [Au(en)$_2$]$^{3+}$ complex (5.85x10^{-3} M) at pH=9.6 and room temperature. After the separation of the gold complex solution by filtration, the solid was washed by deionized water until negative test for chloride ions. The samples were dried at 80^{0}C for 48 h and calcined for 1 h at 400^{0}C. The cationic gold precursor was prepared following the procedure of Block and Bailar [69]. The obtained materials were labeled as Au/xWZ-CP or I, where x stands for the WO$_3$ nominal content in wt %. CP and I denote co-precipitation and impregnation, respectively (see Table 1).

In order to study the effect of tungsten, gold was deposited also on zirconia by cation adsorption of [Au(en)$_2$]$^{3+}$ complex using the same conditions applied to the W-containing samples. Since the incorporation of WO$_x$ species stabilizes the tetragonal phase of zirconia [68,70-76], WO$_x$-free tetragonal zirconia was used for the preparation of ZrO$_2$-supported gold sample. The goal was to eliminate the effect of crystal phase on the interaction of gold precursor with the support because there are differences in the acid-base properties [77], and types and concentration of the surface hydroxyl groups [78] of zirconia polymorphs. In addition, the CO adsorption capacity of monoclinic zirconia is larger than that of the

tetragonal phase [77] which may affect the $CO+O_2$ surface reaction. Li et al. [79] have found that Au supported on monoclinic zirconia exhibited much higher activity in the low-temperature WGS reaction than the catalyst supported on tetragonal zirconia. Tetragonal phase of zirconia was prepared by a method similar to that described by Jung and Bell [78] denoted as procedure 2. The synthesis consisted of hydrolysis of 0.6 M solution of $ZrO_2Cl_2.8H_2O$ with concentrated ammonia solution (25 %) at pH = 9 and room temperature. The obtained precipitate was washed several times with deionized water until negative test for Cl^- ions. Then the washed precipitate was aged in aqueous solution of ammonia (with pH=9) at 100ºC for 48 h under reflux and periodical supplement of $NH_{3(aq)}$ in order to keep constant pH of 9. The resultant hydrated zirconia was dried at 100ºC for 24 h. The material was denoted as HZ-2. Tetragonal zirconia was obtained by calcination of the hydrated zirconia HZ-2 at 600^0C for 6 h.

2.2. Sample characterization

XRD analysis was performed on a Rigaku Miniflex diffractometer with Ni-filtered Cu Kα radiation (λ= 1.5405 Å). The DR-UV-Vis spectra were obtained under ambient conditions with a fiber optic spectrometer AvaSpec-2048 (Avantes) using WS-2 as a reference. The BET surface area measurements were performed with a TriStar 3000 automated gas adsorption analyzer (Micrometics). The samples were dehydrated under vacuum (10^{-2} Torr) for 3 h at 250°C before the measurements in order to remove adsorbed water and volatile compounds. The XRD, DR-UV-vis and BET measurements were performed in the Department of Chemistry, Bilkent University.

The micro-Raman spectra were recorded on a LabRam confocal Raman microscope with a 300 mm focal length (Department of Chemistry, Bilkent University). The spectrometer is equipped with a Ventus LP 532 50 mW diode-pumped solid state laser operated at 20 mW, with a polarization ratio on of 100:1 and a wavelength of a 532 nm and a 1024 x 256 element CCD camera. The signal collected was transmitted via fiber optic cable into a spectrometer with 1800 g/mm grating. The Raman spectra were collected by manually placing the probe tip near the desired point of the sample on a silicon wafer.

The content of gold was determined by ICP-MS analysis in Middle East Technical University, Central Laboratory. The tungsten content in the samples was calculated as difference between the nominal content in the solid and the concentration of tungsten in the filtrate produced during the deposition of gold from the gold precursor. The tungsten content in the filtrate was determined spectrophotometrically by the thiocyanate method at $\lambda = 410$ nm [74,80,81].

The X-ray Photoelectron spectra were obtained using unmonochromatized Al Kα (1486.6 eV) radiation in a VG ESCALAB MK II electron spectrometer (Institute of General and Inorganic Chemistry, Bulgarian Academy of Sciencies) under base pressure of 1×10^{-8} Pa. The spectrometer resolution was calculated from the Ag $3d_{5/2}$ line with the analyzer transmission energy of 20 eV. The half-width of this line was 1 eV. The spectrometer was calibrated against the Au $4f_{7/2}$ line (84.0 eV) and the sample charging was estimated from C1s (285 eV) peak from natural hydrocarbon contaminations on the surface. The accuracy of the binding energy (BE) measured was 0.2 eV. The photoelectron spectra of C 1s, O 1s, Zr 3d, W 4f and Au 4f were recorded and corrected by subtracting a Shirley-type background and quantified using the peak area and Scofield's photoionization cross-sections. The Au particle size was obtained from the XPS peak intensity treated according to the Kerkhof-Moulijn model [82,83].

2.3 FT-IR Spectroscopy

The FT-IR spectra were recorded using a Bomem Hartman & Braun MB-102 model FT-IR spectrometer (Department of Chemistry, Bilkent University) with a liquid-nitrogen cooled MCT detector at a resolution of 4 cm^{-1} (100 scans). The self-supporting discs (~0.01 g/cm^2) were activated in the IR cell by heating for 1 h in a vacuum at 400^{0}C, and in oxygen (100 Torr, passed through a trap cooled in liquid nitrogen) at the same temperature, followed by evacuation for 1 h at 400^{0}C. The spectra of activated sample were taken at high temperature and room temperature (RT), which were used as background references. The spectra of the samples that were subjected to heat treatments at elevated temperatures were recorded at those temperatures. The high temperature background reference was used in the subtraction of the spectra taken at high temperatures and correspondingly the room temperature background reference was used for the spectra registered below 50^{0}C.

2.3.1 Experimental Setup for in situ FT-IR measurements

The IR cell (with BaF$_2$ windows) temperature can be adjusted to high temperatures by electric heater. The sample holder of the cell can be moved vertically with respect to light beam allowing to record also the gas phase spectra (needed for gas phase correction of sample spectra). The IR cell is connected to a vacuum/adsorption apparatus.

2.4 Catalytic activity measurements

The catalytic activity of selected samples in NO reduction by propene was tested in Institute of Nanostructured Materials, CNR, Palermo, Italy using a quartz glass U-shaped reactor, equipped with a temperature programmed controller. All the reactants and products were monitored by IR and UV analyzers. The MS analysis of the reaction products was also performed using online Pfeiffer quadrupole mass spectrometer and Balzers Quadstar software. The steady-state tests were made upon increasing the reaction temperature, waiting at each temperature for a constant conversion value. The catalysts were tested in a wide temperature interval charging 0.100 g of the sample and flow rate of 50 ml/min (STP) corresponding to WHSV of 30000 ml/g·h. Prior to the catalytic testing, the samples were treated "in situ" for 45 min under flowing O$_2$ (5 vol.% in He, 50 ml/min) at 350^{0}C followed by heating for 45 min in He flow at the same temperature. The standard reagent gas mixture contained 1400 ppm of propene, 300 ppm of NO, 4 vol. % of O$_2$ in He.

3. RESULTS AND DISCUSSIONS

It is well known that the activity of the supported Au catalysts strongly depends on the method of preparation [84-86]. The use of careful procedures is critical in order to obtain small gold crystallites well dispersed on the support. It has been found that an optimal gold particle size is between 2 and 5 nm [84,85], although Kung et al. [87,88] reported that maximum activity in the SCR of NO_x with propene over Au/γ-Al_2O_3 catalyst was observed in the 15 to 30 nm particle range. According to Kung et al. [87,88], smaller Au particles appear to favor the combustion of propene lowering the NO_x activity. Also, Seker and Gulari [89] reported very active Au/γ-Al_2O_3 catalyst (~90% of NO_x conversion at ~400^0C) prepared by a sol-gel method and using gold acetate as a precursor. The gold particles in the fresh catalyst had a crystallite size of 37 nm, whereas the size of the gold crystallites in the activated catalyst decreased to 9 nm. This shows that redispersion occurred during the activation step [89].

The simple impregnation of oxide supports with aqueous solutions of $HAuCl_4$ is considered to be an inappropriate path to achieve highly active catalyst. This method results in the formation of large and therefore catalytically inactive gold particles after thermal treatment. Such large particles arise from the too high amount of chlorine residues present in the solids after impregnation, which induce sintering of gold during the activation procedure [90-92].

Among the procedures employed, the deposition-precipitation (DP) method allowed the production of small gold particles and highly active gold catalysts in the extensively studied CO oxidation and WGS reactions [84-86]. An important requirement is that the support materials should have high specific surface area, preferably larger than 50 m^2/g. The DP method enables selective deposition of Au(OH)$_3$ only on the surfaces of the support without precipitation in the liquid phase. Due to the amphoteric properties of Au(OH)$_3$, the pH of aqueous $HAuCl_4$ solution (used as precursor of gold) is adjusted at fixed point in the range of values between 6 and 10 at temperature $50 - 90^0$C. This method, however, is not applicable to metal oxides with isoelectric points (IEP) below 5 [84-86]. Highly dispersed gold nanoparticles ($2 - 5$ nm) cannot be deposited on SiO_2 (IEP = 2 [93]), SiO_2-Al_2O_3 (IEP = 1 [93]), WO_3 (IEP << 3 [93]) or Nb_2O_5 (IEP = 4.1 [93]). The difficulty arises from the tendency of the gold hydroxide species toward agglomeration because of weak interaction of the anionic complex [Au(OH)$_x$Cl$_{4-x}$]$^-$ with the negatively charged surfaces of oxides with low

IEPs [94]. Especially in solution phase, this weak interaction of gold precursor species with the oxide support surfaces is accompanied by a redox reaction under basic conditions [95]. The reduced gold nanoparticles provide the "catalytic" seeds for the uncontrolled aggregation of the gold species.

To overcome the weak interaction of gold species with oxide surfaces having low IEPs, equilibrium adsorption of cationic gold precursor, such as $[Au(en)_2]^{3+}$, has been used to deposit gold on $H_{0.8}Na_{0.2}Y$ zeolite [96,97] and silica [98-100]. The adsorption mechanism of the $[Au(en)_2]^{3+}$ ions involves deprotonated surface hydroxyl groups as anchoring sites [96-100]. The extent of deprotonation depends on the pH of the solution and determines the gold uptake. Maximum gold loading on silica has been achieved at pH = 10.5 resulting in metal particle size of $1.5 - 3.8$ nm [98,100].

The analysis of synthetic conditions for the preparation of highly dispersed gold catalysts leads to the conclusion that the best strategy for the design of gold catalysts supported on tungstated zirconia is to use adsorption of cationic gold precursor.

3.1. Characterization of [Au(en)$_2$]Cl$_3$ precursor solutions

According to Block and Bailar [69] the positive charge density of Au(III) can enhance the acidity of the ethylenediamine ligand (en) and the proton of the amine group can be easily deprotonated under basic conditions. This conclusion is supported by the fact that in the titration of $[Au(en)_2]Cl_3$ with dilute NaOH solution, one equivalent of NaOH was consumed per gold atom, and the solution changed from colorless to yellow above pH of 8 [99,69]. Based on this result Block and Bailer [69] and Zhu et al. [99] concluded that the $[Au(en)_2]^{3+}$ ion undergoes deprotonation under basic conditions as follows:

$$[Au(en)_2]^{3+} + OH^- \rightarrow [Au(en)(NH_2CH_2CH_2NH^-)]^{2+} + H_2O$$
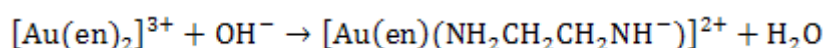
Fig. 1 shows the DR-UV-vis spectrum of the solid $[Au(en)_2]Cl_3$. The strong band with maximum at 302 nm is assigned to the ligand-to-metal charge transfer transition [101,102]. The high intensity of the band suggests that this signal cannot be attributed to the symmetry forbidden d-d transitions [101,102]. The synthesized $[Au(en)_2]Cl_3$ sample was characterized by Raman spectroscopy (Fig. 2). The observed spectrum agrees with that reported by Zanella et al. [98] for the same complex. The bands at 1322 and 1205 cm^{-1} correspond to the ν(C–N) stretching modes. The weak signals between 1000 and 800 cm^{-1} are characteristic to the NH$_2$

wagging and bending vibrations. The group of bands at 476, 343 and 292 cm^{-1} is attributed to Au-N stretching modes. The signal at 520 cm^{-1} belongs to the silicon wafer used for recording the spectrum.
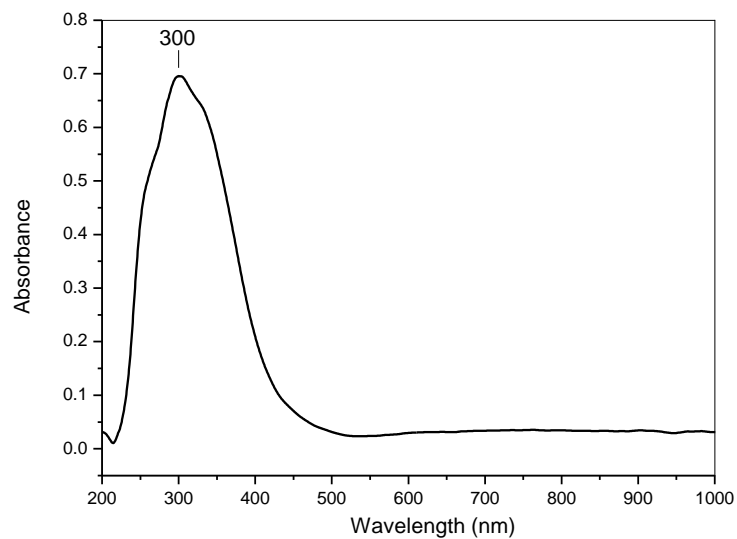
Fig. 1. DR-UV-vis spectrum of [Au(en)$_2$]Cl$_3$
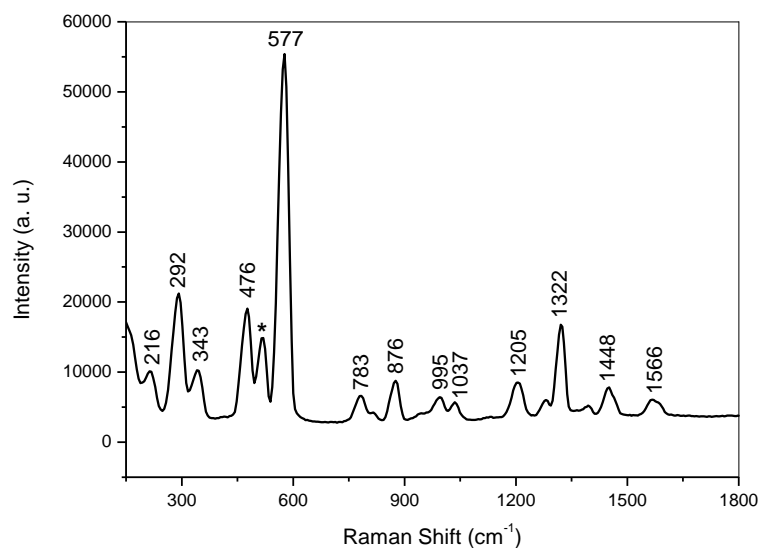
Fig. 2. Raman spectrum of [Au(en)$_2$]Cl$_3$. (the signal marked by asterisk belongs to the Si wafer used for recording the spectrum)

The behavior of the $[Au(en)_2]Cl_3$ precursor solutions at different pH values has been studied and the obtained spectra were compared with those reported by Zhu et al. [99]. Fig. 3 shows that with the increase of the pH from 5.5 to 12.5 a new band at 330 nm appears at lower values of pH which grows in intensity and shifts to approximately 302 nm at pH between 9.6 and 12.5. At the same time the solution changes from colorless to yellow. The appearance of a band at 330 nm is associated with the change of the geometry of $[Au(en)_2]^{3+}$ ion from square planar to pseudo-octahedral due to the formation of axial dative bond with the OH– ions [99,102,103]. The high-energy shift of the absorption from 330 to 302 nm is caused by the formation of the yellow $[Au(en)(en^-)L]^+$ ion ($en^- = H_2NCH_2CH_2NH^-$ and L = Cl^- or OH^-) [99,104]. Chloride ions could be further replaced by hydroxyl groups with increase in the pH. The absorption at 330 nm could be attributed to a d-d transition in a weak ligand field. The spectra shown in Fig. 3 agree well with those reported in the literature [99] and indicate that one hydrogen atom from the $[Au(en)_2]^{3+}$ complex is removed above pH of 8.0 [69,99]. The concentration of the deprotonated gold complex increases with the pH which is evident from the increase in the intensities of the absorption bands. It becomes the dominant species at pH higher than 8. The deprotonated $[Au(en)(en^-)L]^+$ complex at pH = 9.6 has been chosen as precursor for the deposition of gold on the tungstated zirconia because it is expected that the surface concentration of ($M–O^-$) groups (M = Zr, W) to increase with the pH of the deposition solution.

3. 2. Structural characterization

According to the XRD data (Fig. 4) all of the samples studied (except Au/5WZ-I) have the structure of tetragonal zirconia (ICDD Cart No 04-005-4479). The Au/5WZ-I sample contains small amount of monoclinic zirconia (ICDD Cart No 00-013-030).

With increase in the tungsten loading, the analytical content of gold increases (Table 1). It is well known that tungstated zirconia contains acidic protons and their amount increases with the surface density of the WO_x species [67,70,71-74,105]. It is reasonable to propose that as higher the concentration of acidic hydroxyls on the support surface as larger the amount of deprotonated $M–O^-$ surface sites (M = W and Zr) thus leading to greater number of anchoring sites for the $[Au(en)_2]^{3+}$ complex resulting in higher surface concentration of gold. The average size of gold particles, calculated by using Scherrer

equation and the main gold diffraction line of $2\theta = 38.2^0$ (ICDD Cart No 00-004-0784), increases with the W content (Table 1).

The basic medium used for the $[Au(en)_2]^{3+}$ adsorption caused some leaching of WO_x species only in the case of Au/12WZ-I and Au/20WZ-I samples. After the deposition of gold, the tungsten loss amounts to 0.20 ± 0.05 and 0.61 ± 0.02 wt % of WO_3 for Au/12WZ-I and Au/20WZ-I, respectively.

Table 1. Sample notation, BET surface areas, nominal tungsten and analytical gold contents

Sample	S_{BET} (m^2/g)	WO_3 (wt %)	W* (at/nm^2)	Au loading (wt %)	Au loading (at %)	Au particle size (nm)**
Au/ZrO$_2$	143	-	-	1.43±0.03	0.30	8
Au/5WZ-I	116	5.0	1.2	1.27±0.01	0.27	8
Au/12WZ-I	115	11.8	3.0	1.83±0.01	0.40	9
Au/20WZ-I	140	19.4	4.5	2.06±0.03	0.44	10
Au/18WZ-CP	118	18.0	4.8	2.27±0.01	0.48	10

*The W surface density is calculated based on the weight of zirconia; **According to XRD
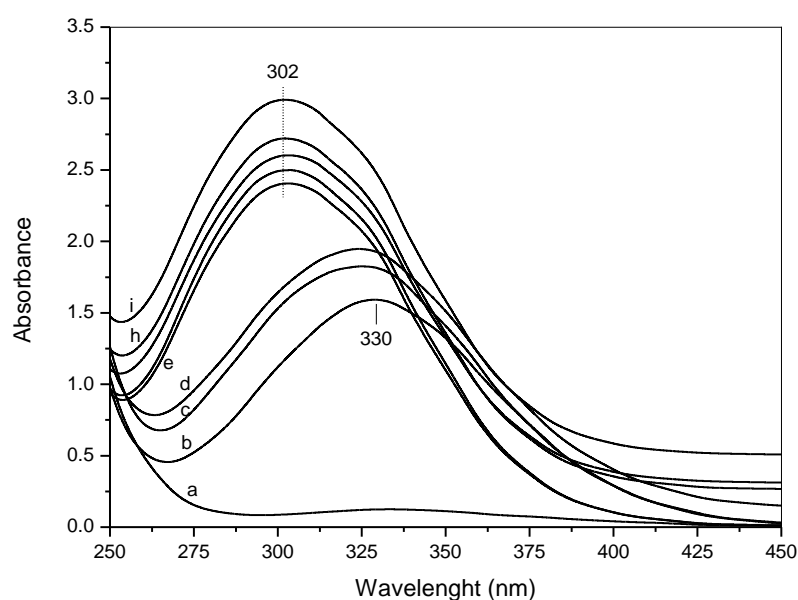
Fig. 3. UV-vis spectra of aqueous solutions of $[Au(en)_2]Cl_3$ ($10{-}4$ M) at different pH values: 5.5 (a); 6.0 (b); 7.0 (c); 8.0 (d); 9.6 (e); 11.0 (f); 11.5 (g); 12.0 (h); i (12.5).
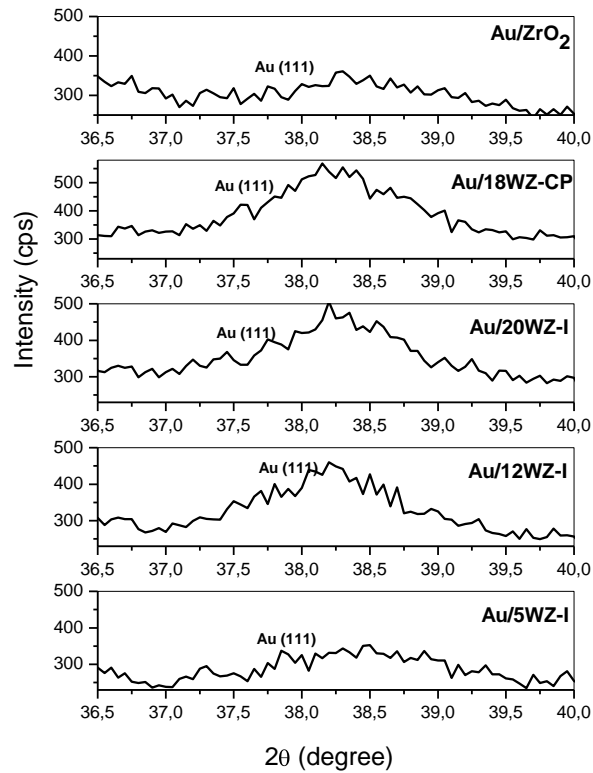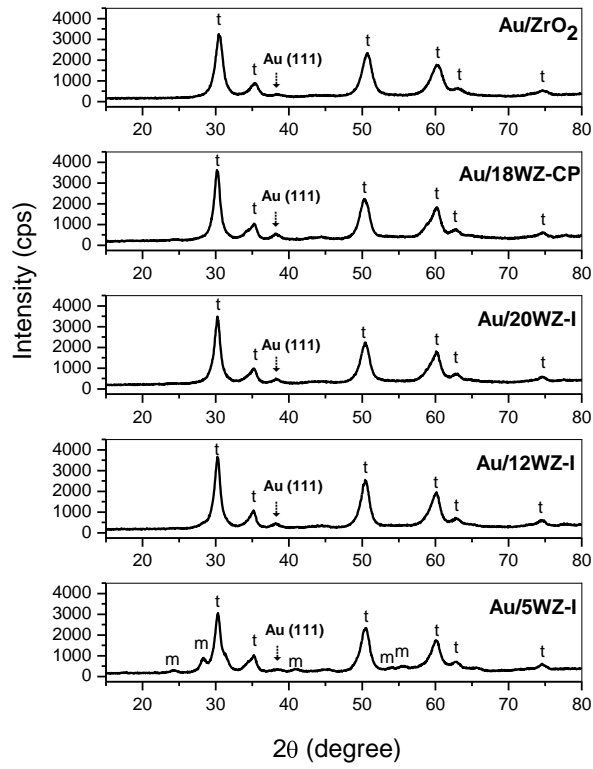
Fig.4. XRD patterns of the samples studied. (t: tetragonal; m: monoclinic)

3.3. DR-UV-vis spectra

Fig. 5 compares the optical spectra of the samples studied. The absorption band at 293 – 270 nm with a shoulder at 260 nm observed in the spectra of the Au-free samples (Fig. 5, spectra (a)) corresponds to LMCT ($O^{2-} \rightarrow W^{6+}$) transition in oligomeric WO_x species with different degree of polymerization [68,71-75]. The introduction of gold causes drastic change in the optical spectra (Fig. 5 spectra (b)). The broad absorption with maximum at 550 nm observed on the gold-containing samples is characteristic of the plasmonic oscillation mode of nanosized gold particles [98,106,107]. The strong band at 270 – 293 nm has disappeared and weak signals at 225 – 230 and 260 – 275 nm are observed instead. Based on the spectrum of Au/ZrO_2 sample (Fig. 5A, spectrum (c)), the former band is attributed to the $O^{2-} \rightarrow Zr^{4+}$ CT transition. The spectra of the Au-containing samples indicate that gold hinders the detection of LMCT transitions. Due to the high absorption coefficient of gold particles [108], they mask the absorption peaks of support. Consequently, the fundamental bands of tungstated zirconia are detected with significantly lower intensities.
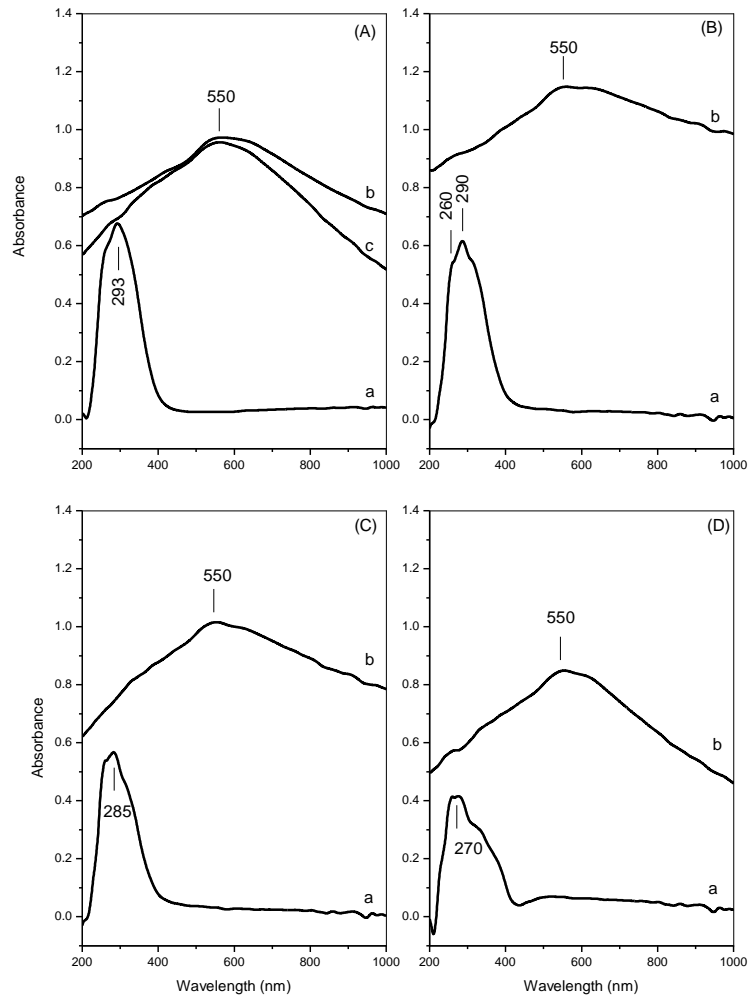
Fig.5. Panel A: Optical spectra of powder samples, 18WZ-CP (a), Au/18WZ-CP (b) and Au/ZrO$_2$ (c). Panel B: Optical spectra of 20WZ-I (a) and Au/20WZ-I (b). Panel C: Optical spectra of 12WZ-I (a) and Au/12WZ-I (b). Panel D: Optical spectra of 5WZ-I (a) and Au/5WZ-I (b).

3.4. XPS analysis

The results of XPS analysis for all samples are summarized in Table 2. Binding energy of $Au4f_{7/2}$ is around 82.8-83.5eV which, in agreement with the literature data on Au/ZrO_2 catalysts [79,109,110-112], is assigned to metallic gold. The full width at half maximum (FWHM) of Au 4f photoelectron line decreases with increasing the WO_3 content. This is a sign of more uniform distribution of Au particles on the W-modified sample surfaces most likely due to the increased gold uptake. The reason for the formation of metallic gold without additional reduction step is the low thermal stability of the $[Au(en)_2]^{3+}$ precursor complex when adsorbed on oxide surfaces [97,98,113]. The initial color of the samples was light yellow, however, during the drying at 80^0C the samples became gray-black. For example the change in the color was faster for Au/5WZ-I than for the Au/ZrO_2 sample. Because both samples have comparable gold loadings it can be suggested that higher W content assists in the decomposition of gold precursor complex.
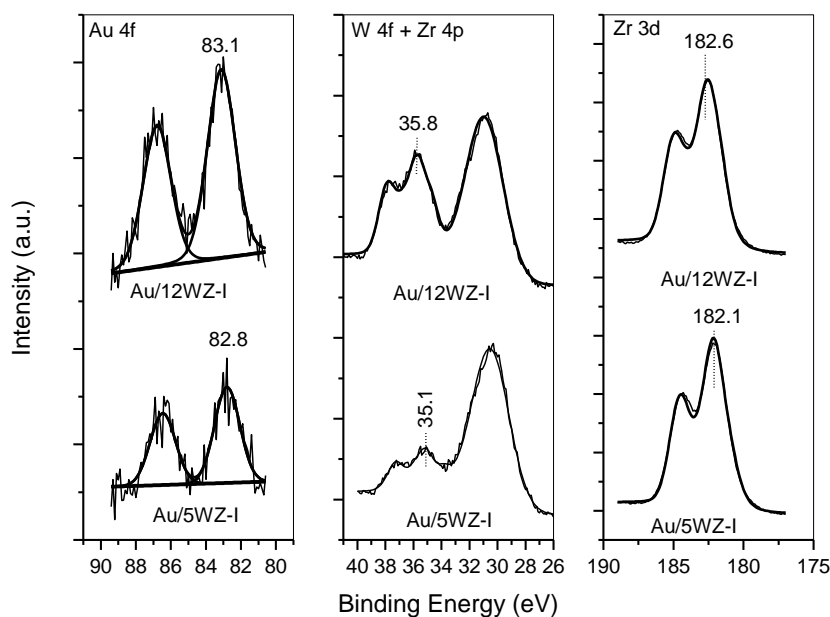
Fig. 6. XP spectra of the Au/5WZ-I and Au/12WZ-I samples showing the Au 4f, W 4f + Zr 4p and Zr 3d regions.

Since the XRD data provide information about the size of large gold clusters (larger than 5 nm [114]), the size of the gold particles was estimated by XPS intensity ratios using the model proposed by Kerkhof and Moulijn [82]. This model is based on the metal loading and specific surface area of the catalysts and is useful for the characterization of very small metal particles [114]. The average particle size calculated from XPS for all gold containing samples is around 3 nm. These results indicate that large (8 – 10 nm) and small (~ 3 nm) gold particles are present on the surfaces of the samples prepared by cationic adsorption of the $[Au(en)_2]^{3+}$ precursor.

Table 2. Binding energies, surface composition and gold particle size for the samples

Sample	O1s		Zr3d$_{5/2}$		W4f$_{7/2}$		Au4f$_{7/2}$			Au particle size, nm
	BE, eV	at %	BE, eV	at %	BE, eV	at %	BE, eV	at %	FWHM*	
Au/ZrO$_2$	530.2	65.2	182.5	34.6	-		82.8	0.2	2.03	2.6
Au/5WZ-I	530.0	63.3	182.1	35.3	35.1	1.2	82.8	0.2	1.87	2.9
Au/12WZ-I	530.5	63.5	182.6	33.9	35.8	2.3	83.0	0.3	1.88	2.8
Au/20WZ-I	530.6	63.0	182.6	33.0	35.9	3.7	83.4	0.3	1.71	3.1
Au/18WZ-CP	530.4	64.7	182.9	32.4	36.3	2.6	83.5	0.3	1.68	3.3

*FWHM for the Au 4f$_{7/2}$ of metallic gold is 1.18 eV

The spectra of the samples (fig. 6) in the W 4f region contain intense doublet with W 4f$_{7/2}$ line at 35.1 – 36.3 eV corresponding to W^{6+} [76,105]. The Zr 3d photoelectron line for all Au catalysts exhibits peak for Zr 3d$_{5/2}$ at 182.0 – 182.9 eV, close to that observed for Zr^{4+} ions [79,105,110,112,115-117]. Fig. 7 shows that the W/Zr surface ratios for the gold catalysts supported on tungstated zirconia prepared by impregnation increases linearly as a function of the tungsten content. This suggests that the dispersion of the WO$_x$ species on the surface of the gold catalysts is uniform [73,76]. For the Au/WZ-CP sample the calculated W/Zr surface atomic ratio deviates from the established linear dependence. It has been shown that all tungsten is located on the surface when tungstated zirconia was prepared by impregnation whereas using co-precipitation results in incorporation of W atoms into ZrO$_2$ lattice, stabilizing the tetragonal structure [70,105].

In the O 1s XPS region an intensive peak at ~530.4 eV is observed for all investigated catalysts. Small asymmetry at higher binding energy side is detected too. This second peak can be related to the existence of O^- ions [118]. This suggests the presence in the subsurface of oxygen ions that bear lower electron density than the "O^{2-}" ions; formally these oxide ions could be described as "O^-" species. They could be associated with sites having higher covalence of the M−O bonds and smaller coordination number of oxygen ions than a regular site. A reasonable hypothesis is to consider the existence, in variable proportions, of defects in the subsurface.
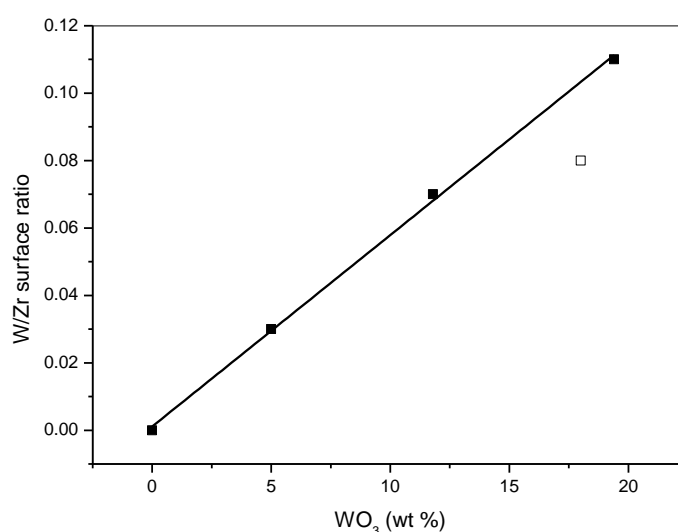
Fig.7. W/Zr surface ratios as a function of WO_3 content in Au/xWZ-I (x = 0, 5, 12 and 20 wt% WO_3) (■) and Au/18WZ-CP samples (□).

The results in Table 2 show that the method of introduction of WO_x species to zirconia (coprecipitation versus impregnation) does not affect the surface concentration of gold. However, in agreement with the chemical analysis, the amount of gold on the surface increases with the WO_3 loading.

3.5. In situ FT-IR spectroscopy

3.5.1. FT-IR spectra of the activated samples

Fig. 8 compares the spectra of the activated Au-free and Au-containing xWZ-I samples. In the OH stretching region all samples of tungstated zirconia contain a band at 3640 – 3635 cm^{-1} which is attributed to W–OH groups [74]. The broad absorption at approximately 3445 cm^{-1} indicates the presence of H-bonded hydroxyls. The spectra in the fundamental W=O stretching region show a sharp band at 1008 – 1002 cm^{-1} typical of W=O species [71,73-75]. The deposition of gold does not cause perturbation of the W=O band. However, compared to the xWZ-I supports, all Au-containing samples display bands in the OH stretching region with lower intensities. This is associated with the involvement of the surface hydroxyls of W-containing supports in the deposition process of gold precursor.
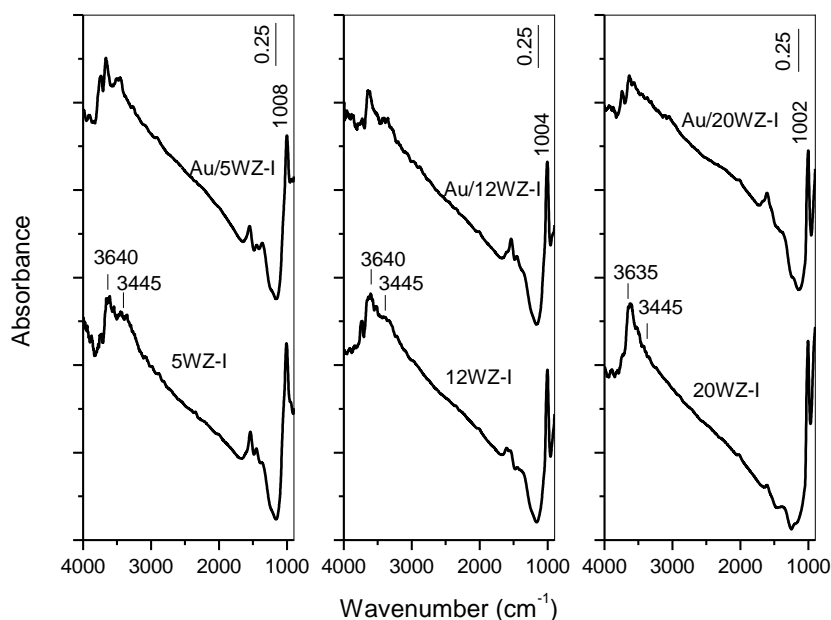
Fig. 8. FT-IR spectra of the activated samples.

26

3.5.2. Adsorption of CO at room temperature

The analysis of the FT-IR spectra of CO (99.95%, BOS) adsorbed at room temperature on the samples can be very useful to obtain qualitative information on the nature of supported gold species. Fig. 9A displays the FT-IR spectra in the carbonyl region of CO (10 Torr) adsorbed on the zirconia samples obtained after the calcination at 600^0C of hydrated zirconias prepared by procedures 1 and 2. The figure shows also the spectra of CO adsorbed on the calcined supports prepared by impregnating the HZ-1 precursor with AMT solution and by coprecipitation. As mentioned above, the samples of zirconia obtained using as precursors hydrated zirconias HZ-1 and HZ-2 crystallize after the calcination at 600^0C in monoclinic and tetragonal structure, respectively. A strong band at 2196 cm^{-1} with a poorly resolved shoulder is observed in the spectrum of CO adsorbed on monoclinic zirconia (Fig. 9A) which corresponds to two types of Zr^{4+}–CO carbonyls [71,74,77,106,119-122]. For the pure tetragonal zirconia sample the CO adsorption yields also one asymmetric band at 2194 cm^{-1} with shoulder at around 2188 cm^{-1} which are ascribed to two types of Lewis acid sites [77,123]. The spectra clearly show that the population of the coordinatively unsaturated (cus) Zr^{4+} sites on monoclinic zirconia is larger than on the tetragonal zirconia. This experimental fact is in agreement with the results of Morterra and coworkers [77] who concluded that morphological and structural reasons are responsible for the different concentration of (cus) Zr^{4+} sites on the surfaces of the two crystallographic modifications of zirconia. Compared to the m-ZrO$_2$, the tungstated samples prepared from the HZ-1 precursor are characterized by lower intensity of the Zr^{4+}–CO band (Fig. 9B) due to saturation of coordinative positions of Zr^{4+} ions in the surface layer by the WO$_x$ species. The intensity of the Zr^{4+}–CO band decreases gradually with increase in the tungsten loading. The high-frequency shift of the carbonyl band exhibited in the WO$_x$-containing zirconia samples is associated with the increased acidity of the (cus) Zr^{4+} sites caused by the electron-withdrawing WO$_x$ groups [71,74]. The intensity of the Zr^{4+}–CO band in all xWZ-I samples (having a tetragonal structure) is significantly higher than that in the pure tetragonal zirconia. This difference can be ascribed to the application of two different procedures for the preparation of the hydrated zirconia used as precursor leading to different morphology of the t-ZrO$_2$ and xWZ-I samples, i.e. different size and shape of the particles, and different amounts of structural defects. In addition, the acidity of the (cus) Zr^{4+} ions located in the proximity of the WO$_x$ domains is enhanced resulting in increased amount of (cus) Zr^{4+} ions detectable by CO adsorption at room temperature.
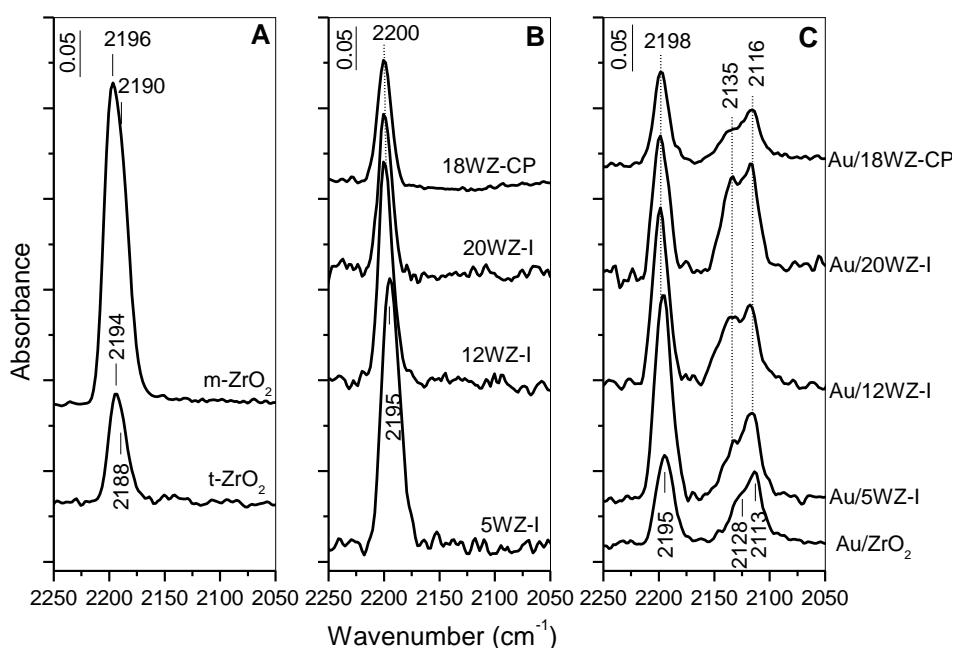
Fig. 9. FT-IR spectra of CO (10 Torr) adsorbed at room temperature on the samples studied. (t: tetragonal; m: monoclinic)

As with the Au-free materials, the absorption at 2195 – 2198 cm^{-1} observed for all Au-promoted samples is assigned to CO adsorbed on Zr^{4+} surface sites (Fig. 9C). The intensity of the Zr^{4+}–CO band in the W-containing samples decreases after the deposition of gold (compare with Fig. 9B) indicating that there are gold nanoparticles located on the zirconia surface. Lower concentration of the (cus) Zr^{4+} ions has been detected also on the surface of Au/ZrO$_2$ sample as compared with the Au-free tetragonal zirconia. According to data from the literature [97,106,119-121,124-128] the absorption with maximum at 2113 – 2116 cm^{-1} is assigned to CO adsorbed on small three-dimensional gold clusters, whereas the shoulder at 2128 – 2135 cm^{-1} is usually attributed to Au$^{\delta+}$–CO species (CO adsorbed on gold clusters with partial positive charge). Formation of positively polarized gold on ZrO$_2$ is assumed to be caused by the presence of adsorbed oxygen on the gold particles or their interaction with the support [106,119,120,124]. Hadjiivanov and coworkers [129,130] proposed that the absorption in the 2155 – 2130 cm^{-1} region could be attributed also to Au^{+}–CO species in which the Au^{+} cation resides on the metallic gold particles. It should be noted that the last

28

activation step of the investigated samples consisted of evacuation at 400^0C and adsorbed oxygen cannot be expected under these conditions. Moreover, after the reduction of the samples at 400^0C with CO, the absorption at $2128 - 2135$ cm^{-1} is still present in the spectra of CO adsorbed at room temperature. Recently, absorption band at $2130 - 2140$ cm^{-1} observed during the CO adsorption on Au/Nb$_2$O$_5$ has been attributed to CO coordinated to larger gold nanoparticles [131]. Therefore, based on the latter interpretation the feature at $2128 - 2135$ cm^{-1} (Fig. 9C) is assigned tentatively to CO coordinated to larger gold nanoparticles. This proposition is supported by the estimates of gold particle sizes from XRD and XPS data showing that the samples have at least two fractions of crystallites, large (~$8 - 10$ nm) and small (~3 nm). For convenience, the absorptions at $2128 - 2135$ cm^{-1} and $2113 - 2116$ cm^{-1} are denoted as high-frequency (HF) and low-frequency (LF) gold carbonyls, respectively. The bands corresponding to the Zr^{4+}–CO and Au–CO species are removed upon dynamic evacuation at room temperature.

According to the chemical analysis the Au loading on Au/ZrO$_2$ and Au/5WZ-I samples is very close, 1.43 and 1.27 wt %, respectively. However, the intensities of the bands due to CO adsorbed on the gold sites are higher for the W-containing sample (Fig. 9C) suggesting higher gold dispersion. Using the same arguments (Au loading and intensities of the Au carbonyl bands), better gold dispersion can be deduced for the Au/20WZ-I (2.06 wt% Au) when compared with the Au/18WZ-CP sample (2.27 wt% Au). The spectra of CO adsorbed on the Au-free supports show that the amount of (cus) Zr^{4+} ions is higher on the 5WZ-I sample than on t-ZrO$_2$. Likewise, the surface concentration of (cus) Zr^{4+} ions on the 20WZ-I sample is higher than that on the 18WZ-CP sample. It can be proposed that the dispersion of gold depends on the amount of (cus) Zr^{4+} ions. This assumption can be supported by the results of Chen and Goodman [132] who showed by using HREELS and CO adsorption that Au bonds directly to coordinatively unsaturated Ti atom on TiO$_2$ (110).

For the Au/xWZ-I sample series, the increase in the intensities of Au carbonyl bands with the amount of tungsten is associated with the increase in the Au loading. According to the results of curve fitting of the gold carbonyl bands (Table 3), the fraction of larger gold particles giving rise to the HF carbonyl band increases with the W loading by larger extent than the fraction of the smaller gold particles characterized by the LF carbonyl band. This experimental fact could be explained by the assumption that in the case of W-containing samples the gold particles formed during the calcination occupy preferentially the WO$_x$-free

29

zirconia surface. The modification of zirconia by tungsten facilitates the gold uptake but at the same time causes decrease in the concentration of (cus) Zr^{4+} ions. The decrease in the amount of nucleation sites for gold particles with increase in the W loading lowers the dispersion.

Table 3. Integrated areas of the gold carbonyl bands recorded at room temperature and $P_{CO}=10$ Torr (see Fig. 8)

Sample	HF Band* (cm^{-1})	I_{HF} (a. u.)	LF Band** (cm^{-1})	I_{LF} (a.u.)	I_{HF}/I_{LF}
Au/ZrO$_2$	2128	0.78	2113	0.97	0.80
Au/5WZ-I	2132	1.28	2115	1.35	0.95
Au/12WZ-I	2136	1.79	2116	1.38	1.30
Au/20WZ-I	2136	2.66	2116	1.53	1.74
Au/18WZ-CP	2134	0.84	2115	0.73	1.15

*HF band corresponds to CO adsorbed on large Au particles;

**LF band corresponds to CO adsorbed on small gold particles.

3.5.3. In situ FT-IR spectroscopic investigation of the NO+O$_2$+C$_3$H$_6$ reaction on the surface of gold catalysts supported on zirconia and tungstated zirconia

In order to evaluate the potential of a new material as catalyst in the process of SCR of NO$_x$, it is important to investigate the interaction of the reactants (C$_3$H$_6$, O$_2$ and NO) with the catalyst surface.

3.5.3.1. NO+O$_2$ surface reaction

Solid Brønsted acids, such as WO$_3$/ZrO$_2$ (~19 % WO$_3$), catalyze the oxidation of NO by molecular oxygen even at room temperature [31]. Fig. 10 shows the spectrum of the gas phase detected at room temperature after 20 min of the admission of a (10 Torr NO (99.9%, Air Products)+25 Torr O$_2$) gas mixture to the IR cell containing Au/ZrO$_2$ sample. Gaseous NO$_2$ (band at 1617 cm^{-1}) and N$_2$O$_4$ (bands at 1758 and 1264 cm^{-1}) are formed by the reaction of NO with O$_2$ in the gas phase (2NO + O$_2$ = 2NO$_2$/N$_2$O$_4$). The exposure of the Au/12WZ-I sample at room temperature to the same gas mixture (Fig. 10) leads to strong increase in the amounts of NO$_2$ and N$_2$O$_4$, which shows that the tungstated zirconia promotes the oxidation

of NO at room temperature. In this process W^{6+} ions are involved [31]. The produced gaseous NO_2 and N_2O_4 adsorb on oxide surfaces with the participation of Lewis acid − base pairs giving rise to surface nitrates and NO^+ species [31,133,134].
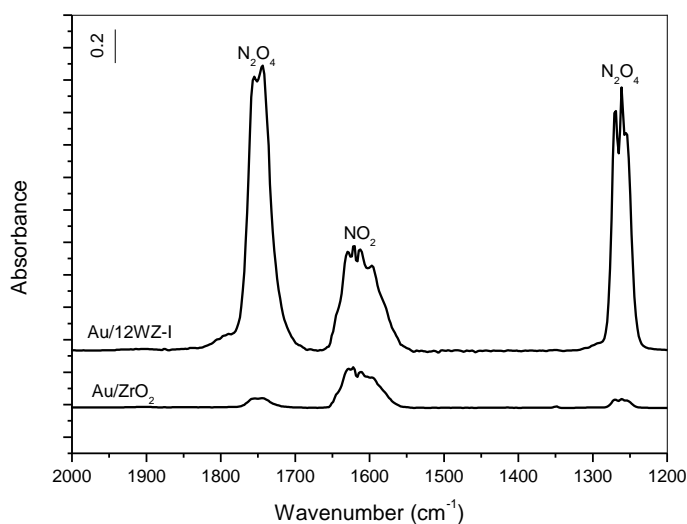
Fig. 10. Gas phase spectra recorded at room temperature after 20 min of the admission of a (10 Torr NO+25 Torr O_2) mixture to the IR cell containing Au/ZrO$_2$ and Au/12WZ-I samples.

In general, the mechanism of SCR of NO_x on various oxide catalysts involves the interaction of strongly adsorbed NO_x^- species (x = 2, 3) with the reducer [17,48,52,135-137]. Therefore we studied the thermal stability of NO_x species adsorbed on the catalyst surfaces. The obtained results are illustrated with the spectra of the Au/ZrO$_2$, Au/12WZ-I, Au/18WZ-CP and 18WZ-CP samples (Fig. 11). NO_x species on the surface of the samples were created by adsorption of a (10 Torr NO + 25 Torr O_2) mixture at room temperature followed by evacuation for 20 min at the same temperature (Fig. 11A-11D, spectra (a)). The absorption bands in the 1700 − 1000 cm^{-1} range are typical of surface nitrates observed on zirconia and tungstated zirconia [31,136,137] and are identified as monodentate (1585 − 1580 and 1275 cm^{-1}) and bidentate (1630 − 1625 and 1230 − 1219 cm^{-1}) NO_3^- species. The broad absorption centered at 2180 − 2140 cm^{-1} is characteristic of NO^+ species [31,136,137]. The spectra clearly show that the intensities of the nitrate bands decreases with increase in the W loading. The modification of zirconia with WO_x species causes lowering of the basicity of the surface O^{2-} ions which leads to decrease in the amount of surface nitrates formed. Heating the

31

isolated IR cell in the $100 - 300^0$C temperature range, leads to gradual decrease in the intensities of the nitrate bands. The spectra of the gas phase (Fig. 11A′-11D′) show that the major product of decomposition of the surface nitrates is NO_2.

There are reports in the literature [130,138], showing that a mixture of $NO+O_2$ can cause oxidation of supported metallic gold particles to cationic gold species and this process can occur at room temperature. In order to find the effect of co-adsorption of $NO+O_2$ mixture on the oxidation state of gold, we investigated the adsorption of CO on the samples containing pre-adsorbed NO_x species. It is well known that the spectral features of adsorbed CO can provide information about the oxidation state of the adsorption site [125]. The results are illustrated with the spectra of the Au/18WZ-CP sample. Surface nitrate species (absorption bands between 1700 and 1000 cm^{-1}) were generated by bringing in contact the Au/18WZ-CP sample with a mixture of 10 Torr of NO and 25 Torr of O_2 for 10 min at room temperature followed by evacuation at the same temperature for 20 min (Fig. 12, spectrum (a)). To the sample treated in this way, 10 Torr of CO were added. The spectrum detected at room temperature after 5 min contains a strong band with maximum at 2185 cm^{-1} (Fig. 12, spectrum (b)). The intensity of this signal increases significantly after 10 min of contact with the CO (Fig. 12, spectrum (c)). Weak absorption at 2130 cm^{-1} is observed as well whose intensity increases in parallel with the main band at 2185 cm^{-1}. The latter signal falls in the range of reported ν(CO) stretching vibrations of Au^+–CO species (2197 – 2160 cm^{-1} [125,129,130,138-141]). However, the increase in the intensity of the band at 2185 cm^{-1} during the contact with CO contradicts the observed instability of the Au^+–CO species in CO atmosphere [138-141] due to reduction of Au^+ adsorption sites by CO.
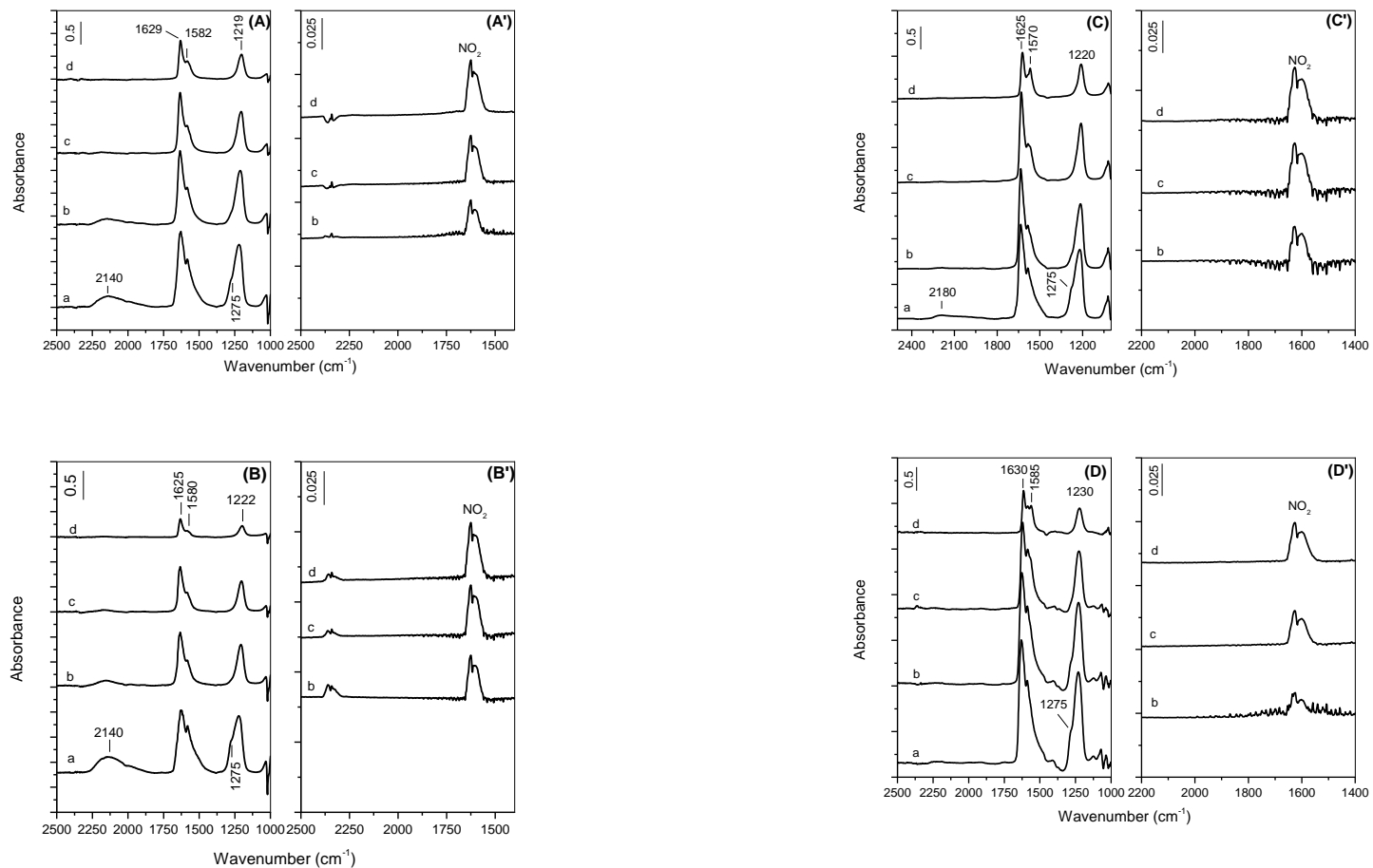
Fig. 11. FT-IR spectra of the Au/18WZ-CP (panel A), 18WZ-CP (panel B), Au/12WZ-I (panel C) and Au/ZrO$_2$ (panel D) samples taken after the introduction of a (10 Torr NO+25 Torr O$_2$) mixture to the IR cell for 10 min at room temperature followed by evacuation for 20 min (a), and after heating the isolated IR cell for 10 min at 100^{0}C (b), 200^{0}C (c) and 300^{0}C (d). Panels A′, B′, C′ and D′: Gas phase spectra over the samples collected at 100^{0}C (b), 200^{0}C (c) and 300^{0}C (d).
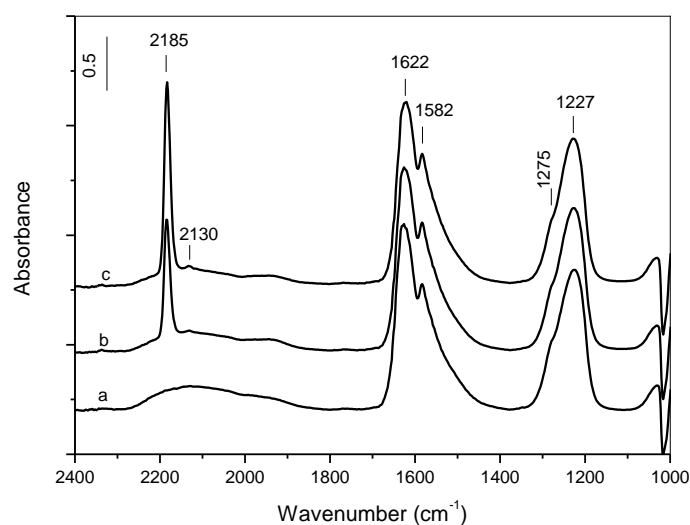
Fig. 12. FT-IR spectra of the Au/18WZ-CP catalyst collected after the adsorption of a (10 Torr NO + 25 Torr O_2) mixture for 10 min at room temperature followed by evacuation for 20 min at room temperature (a) and adsorption of 10 Torr CO at room temperature for 5 min (b) and 10 min (c).
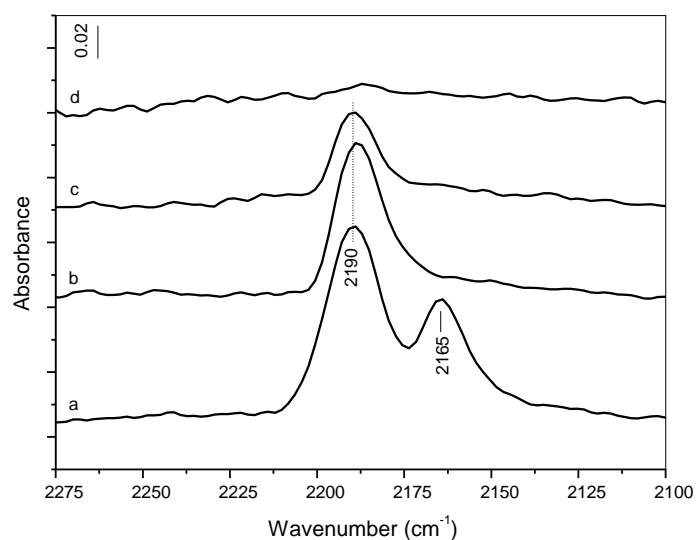
Fig. 13. FT-IR spectra of the Au/18WZ-CP sample collected after the adsorption of a (10 Torr NO + 25 Torr O_2) mixture for 30 min at 300^0C followed by dynamic evacuation from 200^0C to room temperature and subsequent adsorption of 10 Torr of CO for 10 min (a), evacuation for 15 min at room temperature (b), 50^0C (c) and 100^0C (d).

34

In order to ensure more efficient oxidation of gold, the catalyst pellet was treated with a (10 Torr NO + 25 Torr O_2) mixture at 300^0C for 30 min. Then the temperature was lowered to 200^0C and the gas mixture was removed from the IR cell upon dynamic evacuation while cooling to room temperature. Subsequent adsorption of CO (10 Torr) at room temperature results in the formation of weak absorption bands at 2190 and 2165 cm^{-1} (Fig. 13, spectrum (a)). The spectrum in the nitrate region (not shown) displays the same set of nitrate bands as shown in Fig. 11A, although with weaker intensity. The band at 2190 cm^{-1} resists the evacuation at room temperature (Fig. 13, spectrum (b)) and disappears upon out-gassing at 100^0C (Fig. 13, spectrum (d)). The observed behavior of the absorption at 2190 cm^{-1} is typical of Au^+–CO species [125]. The CO adsorbed on Au^+ sites is stabilized by the synergism between the δ-dative and π back-bonding components of the Au^+–CO bond [125,129,130,138] and the carbonyl complex can be destroyed at temperature higher than 25^0C. The absorption at 2165 cm^{-1} disappears upon evacuation at room temperature (Fig. 13, spectrum (b)) and could be attributed to $Au^{\delta+}$–CO species or CO adsorbed on large gold particles. This band is found at higher frequency than the corresponding band observed on the activated Au/18WZ-CP sample (see Fig. 9C) indicating that either the $Au^{\delta+}$ sites bear a greater positive charge or there is agglomeration of the gold particles after the high-temperature treatment with NO+O_2 mixture. It is likely that the species giving rise to the band at 2165 cm^{-1} could be Au^+ adsorption sites dispersed on the surface of metallic gold particles as proposed in [129,130].

Spectrum (a) in Fig. 13 differs from the spectrum of adsorbed CO on the sample treated with NO+O_2 mixture at room temperature (Fig. 12, spectrum (c)). It seems that the oxidation of gold particles by the NO+O_2 mixture takes place at higher temperature (300^0C) and the absorption band at 2185 cm^{-1} detected during the CO adsorption on the sample treated with NO+O_2 mixture at room temperature (Fig. 12, spectra (b) and (c)) cannot be ascribed to Au^+–CO species. This conclusion is supported also by the fact that the color of the Au/18WZ-CP sample after the pre-treatment with NO+O_2 mixture at room temperature remained the same as that of the activated sample, i.e. gray-black. However, the treatment with NO+O_2 mixture at 300^0C causes changes in the color of the sample from gray-black to pale-violet (Au^+).

Taking into account that the compounds adsorbed at room temperature on the Au/18WZ-CP sample are CO and NO_x species, it could be proposed that the strong band at

2185 cm^{-1} in Fig. 12 could be attributed to NCO species formed on metallic gold sites. According to the literature [126,142,143] the Au–NCO species give rise to absorption band at 2180 – 2190 cm^{-1}. In order to verify this assumption we performed ^{13}CO adsorption on the sample treated with NO+O$_2$ mixture at room temperature (Fig. 14). The band at 2185 cm^{-1} is shifted down by 57 cm^{-1} and is positioned at 2128 cm^{-1} on ^{13}C substitution. The observed $\Delta\nu$ value is consistent with that reported by Celio et al. [144] for the isotopic shift detected on substituting ^{13}C for ^{12}C in NCO species adsorbed on Cu(100). From these results it can be concluded that the weak absorption at about 2130 cm^{-1} in Fig. 12, spectrum (c) belongs to the ^{13}CO satellite of the band at 2185 cm^{-1}.
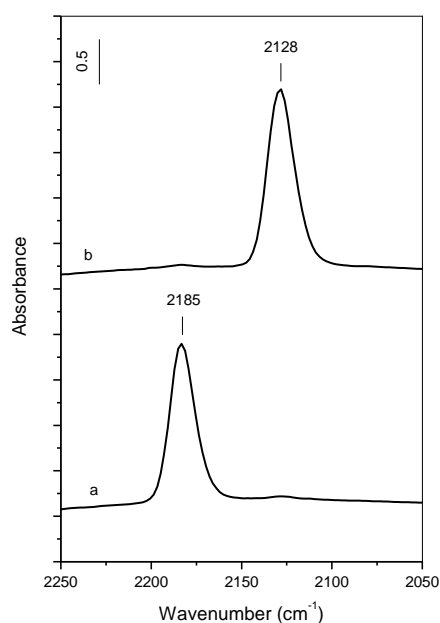
Fig. 14. FT-IR spectra of 10 Torr of CO (a) and 10 Torr of ^{13}CO (b) adsorbed at room temperature on the Au/18WZ-CP sample containing pre-adsorbed NO$_x$ species.

The behavior of the absorption at 2185 cm^{-1} in the presence of water vapor can be used as additional evidence supporting the assignment of this feature to Au–NCO species. It is well known that the NCO species can react with water producing ammonia and CO$_2$ through the formation of HNCO [145,146]. The species characterized by the absorption band

at 2185 cm^{-1} are generated by adsorption of CO (10 Torr, for 10 min) on the sample treated with NO+O$_2$ mixture at room temperature as described above and then the gaseous CO was evacuated for 15 min (Fig. 15A, spectrum (a)). The addition of 0.1 Torr of water vapor at room temperature causes significant decrease in the intensity of the band at 2185 cm^{-1} (Fig. 15A, spectrum (b)) and appearance of CO$_2$ and HNCO (ν_{as}(NCO) at 2266 cm^{-1} [52]) in the gas phase (Fig. 15B, spectrum (b)). The formation of the latter compounds confirms unambiguously the assignment of the band at 2185 cm^{-1} to Au−NCO species. Increasing the temperature to 100^{0}C results in further decrease in the amount of isocyanates (Fig. 15A, spectrum (c)) and they disappear completely at 200^{0}C (the spectrum is not shown). No ammonia was detected in the gas phase most likely because of its low concentration and/or adsorption on the catalyst surface. The sample spectra in the NH stretching region are noisy and are not informative. The bending modes of coordinated ammonia and NH$_4^+$ ion fall in the region of stretching vibrations of the nitrates and if formed, they cannot be resolved. It should be noted that the adsorption of CO on the NO$_x$-precoved 18WZ-CP sample does not lead to the formation of NCO species which on oxides surfaces produce absorptions in the 2280 − 2200 cm^{-1} region [126,137,142,143,147]. The absence of NCO species coordinated to the support in the case of Au/18WZ-CP sample can be explained by unavailability of adsorption sites which are blocked by the nitrate species.

Fig. 15. Panel A: FT-IR spectra of the Au/18WZ-CP catalyst collected after the adsorption of (10 Torr NO + 25 Torr O$_2$) mixture for 10 min at room temperature followed by evacuation for 20 min at room temperature, adsorption of 10 Torr CO at room temperature for 10 min and evacuation of the gaseous CO for 15 min (a), and subsequent addition of 0.1 Torr of water vapor for 10 min at room temperature (b) and 100^{0}C (c). Panel B: Gas phase spectra corresponding to the sample spectra (b) and (c).

The Au−NCO species observed on the Au/18WZ-CP sample are characterized by a high thermal stability and they are removed by dynamic evacuation at 350^0C (Fig. 16).

The NCO species are considered as reactive intermediates in the selective reduction of NO_x [17,36,48,58,126,148-151]. The spectra shown in Fig. 17 illustrate the reactivity of the Au−NCO species generated on the Au/18WZ-CP sample toward NO_2. The NCO species have been obtained by adsorption of 10 Torr of CO on the NO_x-precovered Au/18WZ-CP sample followed by evacuation for 20 min at room temperature (Fig. 17, spectrum (a)). After the admission of 0.4 Torr of NO_2 at room temperature (Fig. 17, spectrum (b)), the isolated IR cell was heated between 25 and 250^0C for 10 min at each temperature. The exposure of the sample to NO_2 at room temperature (Fig. 17, spectrum (b)) causes strong decrease in the intensity of the band at 2185 cm^{-1} indicating that the NCO + NO_2 reaction takes place already at 25^0C. The surface concentration of the NCO species decreases rapidly with the temperature and they disappear at 250^0C (Fig. 17, spectrum (g)). The gas phase spectra (not shown) contain CO_2 and NO_2 that has been taken in excess. As shown above, the Au−NCO species have high thermal stability and leave the surface upon dynamic evacuation at 350^0C (Fig. 16). The generation of Au−NCO species by interaction of CO with adsorbed NO_x species suggests that Au supported on tungstated zirconia might be used as catalyst for the selective reduction of NO_x by CO.
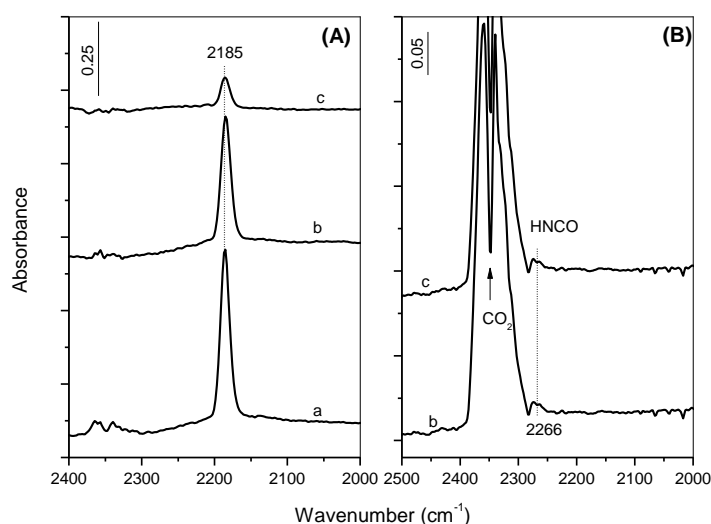
Fig. 16. FT-IR spectra of the Au/18WZ-CP catalyst collected after the adsorption of a (10 Torr NO + 25 Torr O_2) mixture for 10 min at room temperature followed by evacuation for 20 min at room temperature, then adsorption of 10 Torr CO at room temperature for 10 min and evacuation of the gaseous CO for 15 min at various temperatures (RT = room temperature).
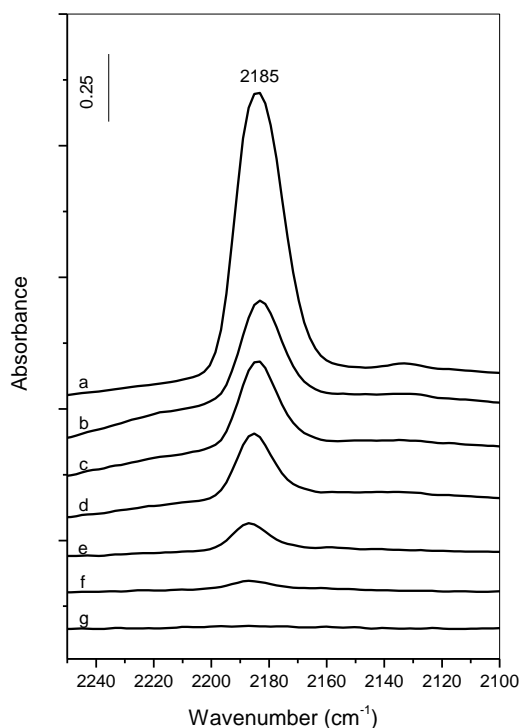
Fig. 17. FT-IR spectra of the Au/18WZ-CP catalyst collected after the generation of the Au−NCO species (a) (for the conditions see Fig.10, spectrum (RT)) and subsequent addition of 0.4 Torr of NO_2 for 10 min at 25^0C (b), 50^0C (c), 100^0C (d), 150^0C (e), 200^0C (f) and 250^0C (g).

The adsorption of CO on gold catalysts supported on tungstated zirconia obtained by impregnation (Au/xWZ-I samples, x = 5, 12 and 20 wt % WO_3) and containing pre-adsorbed NO_x species leads also to the formation of NCO species coordinated to gold particles. As with the Au/18WZ-CP sample, surface nitrates on the Au/xWZ-I samples were created by adsorption of mixture of 10 Torr NO and 25 Torr O_2 at RT for 10 min followed by evacuation for 20 min at RT. Fig. 18 compares the FT-IR spectra obtained during the CO adsorption for 10 min at 50^0C over the NO_x-pretreated Au/xWZ-I and Au/18WZ-CP samples. This temperature has been chosen because under these conditions the Au−NCO band at 2185 cm^{-1} observed on all of the samples reaches maximum intensity. The spectra clearly show that the intensities of the nitrate bands at 1625, 1583, 1275 and 1225 cm^{-1} decreases with increase in the W loading which is consistent with the reduced surface basicity. The lower intensity of the Au−NCO band on the samples with higher tungsten content is associated with the decrease in the gold dispersion.
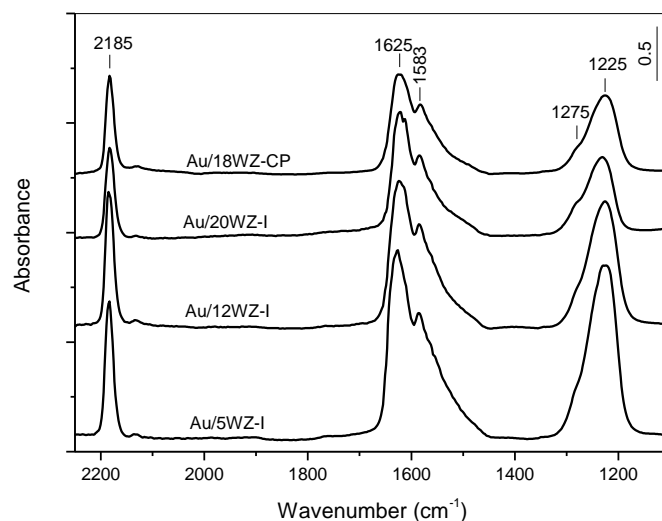
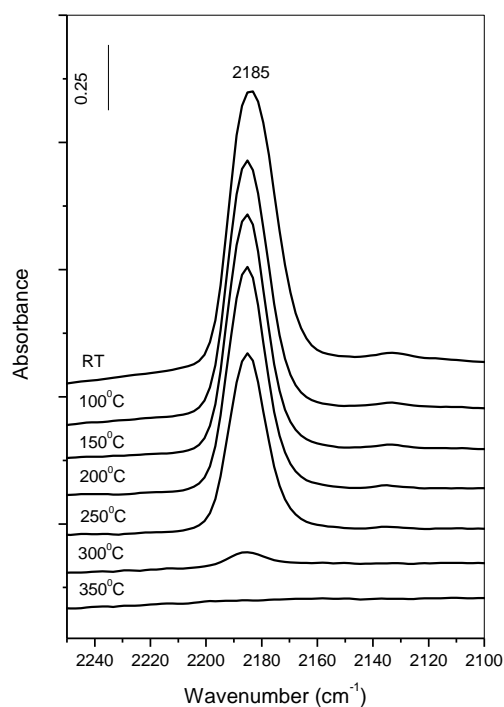Fig. 18. FT-IR spectra of the samples collected after the adsorption of a (10 Torr NO + 25 Torr O_2) mixture for 10 min at room temperature followed by evacuation for 20 min at room temperature and adsorption of 10 Torr CO at 50^0C for 10 min.

It is difficult to propose unambiguous mechanism for the formation of NCO species on the gold-containing catalysts. Jugnet et al. [152] reported that CO undergoes disproportionation on Au(110) surface at room temperature. We believe that this process is also occurring on the Au/xWZ-I samples. The produced carbon can interact with the surface nitrates leading to the formation of NCO species attached to the gold sites.

3.5.3.2 Co-adsorption of $C_3H_6+O_2$ mixture on the Au/ZrO$_2$ and Au/xWZ-I catalysts at various temperatures

In this investigation we used the gold catalysts supported on tungstated zirconia prepared by impregnation. In order to find information about the effect of tungsten, the $C_3H_6+O_2$ reaction has been studied on the Au/ZrO$_2$ sample as well.

Fig. 19 shows the spectra in the $25 - 300^0C$ temperature range obtained during the contact of the Au/ZrO$_2$ and Au/xWZ-I catalysts with a gas mixture containing 3 Torr of C_3H_6 and 25 Torr of O$_2$. The spectrum of the Au/ZrO$_2$ sample taken at room temperature (Fig. 19A, spectrum (a)) contains absorptions at 1620 and 1453 cm^{-1} characteristic of adsorbed propene [18,153]. Heating the closed IR cell at 150^0C causes oxidation of the hydrocarbon leading to formation of polydentate carbonates at 1445 and 1420 cm^{-1} [154,155] and most likely HCO$_3^-$ species at 1610 and 1270 cm^{-1} [154,155]. Small amounts of adsorbed acetone at 1670 cm^{-1}[18,29,30,156-158] and most likely acetates at 1562 and 1368 cm^{-1} [18,29,30] are detected as well. At 250^0C the adsorbed acetone disappears and the predominant adsorbed species are the acetates at 1562, 1445 and 1368 cm^{-1}. The experimental results lead to the conclusion that the W-free Au/ZrO$_2$ sample catalyzes the deeper oxidation of propene. The assignment of the absorption bands is given in Table 4.

The spectra of the Au/xWZ-I samples (Figs. 19B-19D) taken at room temperature contain also bands at 1620, 1454 – 1450 and 1375 cm^{-1} corresponding to adsorbed propene. The weak absorption at 1090 cm^{-1} detected in the spectrum of the Au/20WZ-I sample (Fig. 19D, spectrum (a)) indicates the presence of isopropoxy species which are produced by interaction of propene with the surface OH groups [18,29,30,156,157,159-161]. The absorption at 1540 cm^{-1} (Fig. 19D, spectrum (a)) is best assigned to acetone enolate anion [29]. Formation of partially oxidized hydrocarbons on the Au/20WZ-I sample at room temperature indicates that the activation of propene takes place easy on this material. Heating

the closed IR cell at 150^0C for 10 min (Figs. 19B-19D, spectra (b)), results in disappearance of the adsorbed propene and bands corresponding to adsorbed acetone and acetate species are observed for all of the Au/xWZ-I samples. This result is in agreement with the fact that the presence of Brønsted acidity combined with redox sites [18,29,30] such as W=O groups facilitate the partial oxidation of propene. The amount of the adsorbed acetone increases with the temperature being the highest on the Au/12WZ-I and Au/20WZ-I samples. The assignment of the absorption bands is shown in Table 5.

Table 4. Assignments of the adsorption bands in the spectra observed during the high-temperature adsorption of $C_3H_6 + O_2$ mixture on the Au/ZrO$_2$ catalyst.

Species	Band position, cm^{-1}	Vibration
C_3H_6 (ads)	1620, 1453	ν(C=C), δ_{as}(CH$_3$)
polydentate CO_3^{2-}	1445, 1420	ν_{as}(CO$_2$), ν_s(CO$_2$)
Bidentate HCO_3^{-}	1610, 1270	ν_{as}(CO$_2$), δ(OH)
Acetone (ads)	1670	ν(C=O)
CH_3COO^{-}	1562, 1445, 1368	ν_{as}(COO), ν_s(COO), δ(CH$_3$)

Table 5. Assignments of the adsorption bands in the spectra observed during the high-temperature adsorption of $C_3H_6 + O_2$ mixture on the Au/xWZ-I catalysts.

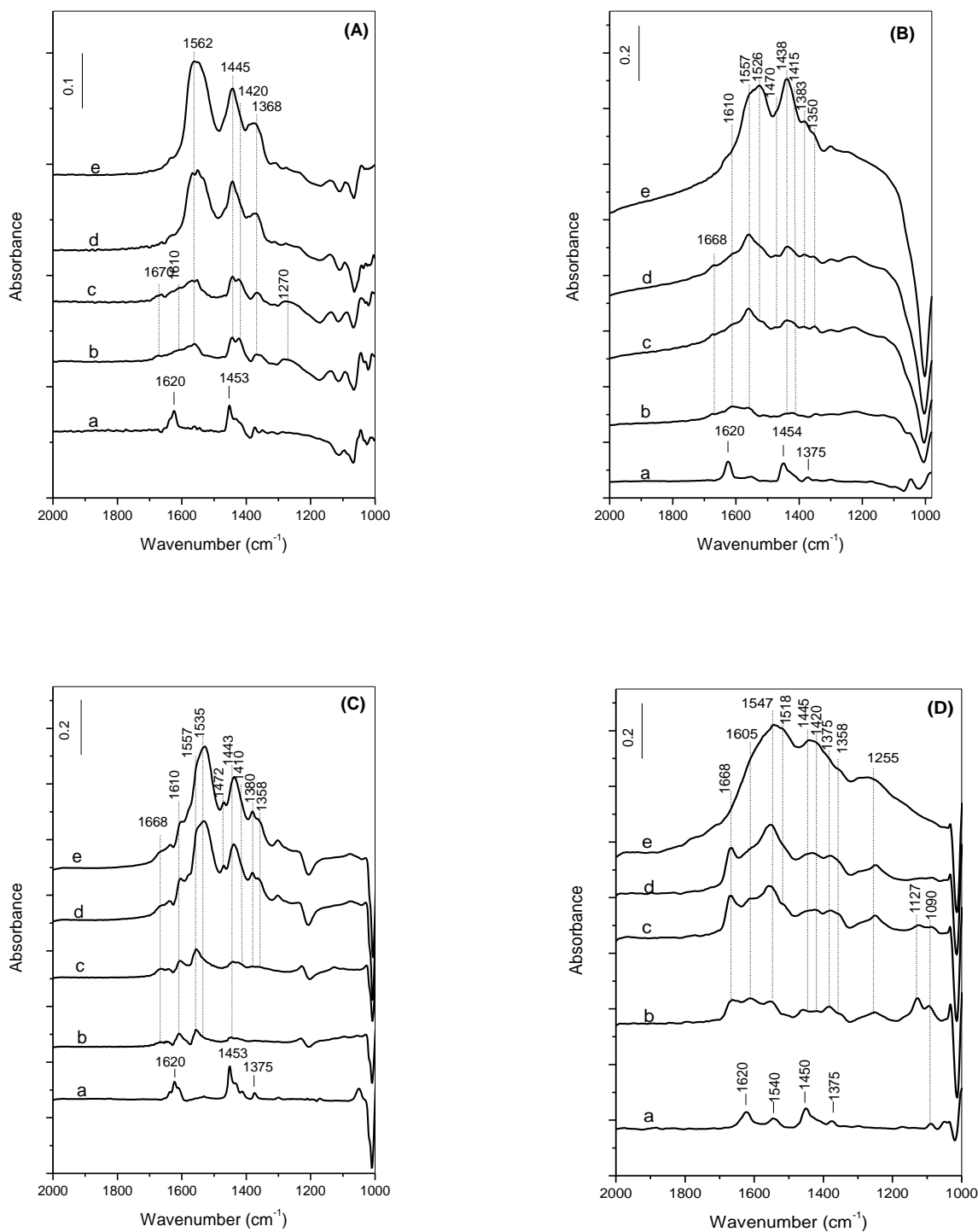| Species	Band position, cm^{-1}	Vibration
C_3H_6 (ads)	1620	ν(C=C)
	1454-1450	$\delta_{as}(CH_3)$
	1375	$\delta_s(CH_3)$
Isopropoxide (two types)	1127, 1090	ν(C−O)
Acetone enolate anion	1540	$\nu_{as}(^-O-C=C/O=C-C^-)$
Acetone (ads)	1668	ν(C=O)
	1255	ν(CCC)
CH_3COO^-	1610-1605, 1557-1547, 1535-1518	$\nu_{as}(COO)$
(three types)	1472-1470, 1445-1438, 1420-1410	$\nu_s(COO)$
	1383-1375, 1358-1350	$\delta(CH_3)$

Fig. 19. FT-IR spectra collected during the exposure of the Au/ZrO$_2$ (Panel A), Au/5WZ-I (Panel B), Au/12WZ-I (Panel C) and Au/20WZ-I (Panel D) catalysts to a (3 Torr C$_3$H$_6$ +25 Torr O$_2$) mixture for 10 min at room temperature (a) followed by heating the isolated IR cell for 10 min 150^{0}C (b), 200^{0}C (c), 250^{0}C (d) and 300^{0}C (e).

3.5.3.3. Reactivity of the surface species formed upon room-temperature adsorption of NO+C₃H₆+O₂ mixture on Au/xWZ-I catalysts

It has been shown previously that the conversion of propene to acetone in the presence of acidic catalyst is important step in the SCR of NO_x by propene [18]. Therefore, here we will describe the results of in situ FT-IR spectroscopic investigation of the NO_x+C_3H_6 surface reaction over the Au/12WZ-I and Au/20WZ-I catalysts.

Fig. 20A shows the spectrum of the Au/12WZ-I sample exposed to a gaseous mixture containing 10 Torr NO + 3 Torr C_3H_6 + 25 Torr O_2 at room temperature for 15 min followed by evacuation for 20 min (spectrum (a)). The broad absorption between 3550 and 3000 cm^{-1} is typical of H-bonded hydroxyls and indicates that the oxidation of propene has occurred already at room temperature. The weak bands at 3006 and 2990 cm^{-1} are assigned to the ν(CH) and ν_s(CH$_2$) modes of adsorbed propene [18,153] while the absorptions at 2938 and 2875 cm^{-1} are attributed to the ν_{as}(CH$_3$) and ν_s(CH$_3$) stretching vibrations of adsorbed propene [18,153] and partially oxidized derivatives of the hydrocarbon [18,29,30, 156,157,159-161]. The bands in the 1800 – 1000 cm^{-1} region differ from that observed upon NO+O$_2$ adsorption (see Fig. 11) which suggests that the presence of adsorbed propene and its products of oxidation influence the mode of coordination of the nitrate species. The bands at 1654 and 1255 cm^{-1} are assigned to bridged nitrates whereas the bands at 1605, 1577 and 1278 cm^{-1} are attributed to bidentate nitrates. The weak absorptions at 1138 and 1090 cm^{-1} reveal the presence of isopropoxides and correspond to their ν(C–O) modes [18,29,30, 156,157,159-161]. The unresolved absorption at 1680 cm^{-1} belongs to the ν(C=O) stretching vibration of adsorbed acetone [18]. The fact that no partially oxidized hydrocarbon species were observed at room temperature during the C$_3$H$_6$+O$_2$ experiment (Fig. 19C, spectrum (a)), indicates that the formation of surface nitrates and/or gaseous NO$_2$ during the room-temperature adsorption of NO+C$_3$H$_6$+O$_2$ mixture facilitates the activation of propene.

Heating the sample for 15 min at 100^{0}C leads to the appearance of a shoulder at 1730 cm^{-1} which has been attributed previously [18] to the ν(C=O) mode of adsorbed nitroacetone. This compound is formed most likely by interaction of the isopropoxides with the NO$_3^-$/NO$_2$ species. The appearance of weak bands at 1470, 1440, 1380 and 1350 cm^{-1} indicate the formation of two types of acetate species [18,30,156-158]. The concentration of the surface

nitrates has decreased and the amount of NO_2 evolved in the gas phase (Fig. 20B, spectrum (b)) is much smaller than that produced in the absence of propene (Fig. 11C′, spectrum (b)). Some amounts of N_2O and CO_2 are formed as well. The presence of CO_2 in the gas phase indicates that complete oxidation of propene takes place to some extent at 100^0C. At 150^0C (Fig. 20, spectra (c)), the intensities of the nitrate bands at 1278 and 1255 cm^{-1} and the amount of gaseous NO_2 decrease significantly. At the same time, there is increase in the amounts of adsorbed nitroacetone (1730 cm^{-1}), acetone (shoulder at 1680 cm^{-1}) and acetates (absorptions between 1500 and 1300 cm^{-1}). The lowering of the concentrations of the isopropoxides (1138 and 1090 cm^{-1}) and gaseous NO_2 indicates that they are involved in the formation of the carbonyl compounds, which are further oxidized to acetates. The weak band at 2182 cm^{-1} detected at 150^0C is attributed to NCO species coordinated to gold particles [126,142,143]. Increasing the temperature to 200^0C leads to broadening of the Au−NCO band and unresolved shoulder at ~2150 cm^{-1} is observed. It can be proposed that the NCO species coordinated to small and large gold particles produce v_{as}(NCO) vibrations at different frequencies. Assuming that the larger gold particles are less reactive, the low-frequency Au−NCO band at 2150 cm^{-1}, which appears at higher temperature, can be attributed to NCO species coordinated to larger metal clusters. The spectrum taken at 200^0C indicates that the amount of adsorbed nitroacetone decreased relative to that at 150^0C. This leads to the conclusion that the generation of Au−NCO species takes place through transformation of nitroacetone. Allesandrini et al. [162] have shown that complexes of Pt(II) and Pt(0) can cause cleavage of α-nitroketones resulting in metal complexes containing fulminato and carboxylato groups. The coordinated fulminato (CNO) species can undergo isomerization to isocyanates (NCO). It can be proposed that Au particles are involved in a similar internal redox process of nitroacetone resulting in Au−NCO species formation:

$$O=N-O\cdots Au \longrightarrow Au\text{-}NCO^- + CH_3COO^- + 2H^+ \qquad (1)$$
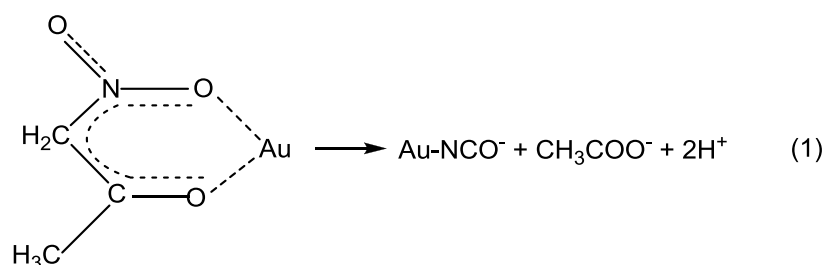
The surface isocyanates react readily with $NO+O_2$ mixtures and/or NO_2 yielding molecular nitrogen, N_2O and CO_2 as reaction products [17,18,42,43,137,149,151,163,164]. This fact can account for the disappearance of the NCO species and strong decrease in the

amount of surface nitrates (which are source of NO_2) at 250^0C. The spectrum detected at 300^0C contains bands at 1535, 1440 and 1350 cm^{-1} due to surface acetates and carbonates. The carbonates are formed by readsorption of the CO_2 which is supported by the observed lowering of its concentration in the gas phase at 300^0C (Fig. 20B, spectrum (f)). The assignment of the absorption bands is given in Table 6.

Fig. 21 shows the results of the reactivity of surface species formed upon room-temperature adsorption of ($NO+O_2+C_3H_6$) mixture on the Au/20WZ-I catalyst in the 25 – 250^0C temperature range. The experimental conditions are the same as those for the Au sample containing 12 wt % of WO_3. The gas phase spectra and the band envelope in the 1800 – 1000 cm^{-1} range at different temperatures (Fig. 21) are similar to those observed for the Au/12WZ-I sample. The assignment of the absorption bands is shown in Table 6. The following differences should be noted:

1. The spectra in the ν(OH) stretching region are practically unperturbed, which indicates that complete oxidation of propene does not take place. This conclusion is supported by the fact that CO_2 is detected in the gas phase at 200^0C and higher temperatures when the interaction between the surface nitrates, respectively activated NO_2, and the Au–NCO species takes place.
2. The amount of isopropoxide species (observed at 1138 and 1090 cm^{-1}) formed at room temperature is significantly larger on the sample containing 20 wt % WO_3 than on the Au/12WZ-I catalyst. In addition, the spectrum taken at room temperature (Fig. 21A, spectrum (a)) shows the presence of nitroacetone. These observations are in agreement with the conclusion made above that the high WO_3 content facilitates the partial oxidation of propene.
3. The surface nitrates of the Au/20WZ-I catalyst disappear at 200^0C whereas in the case of the Au/12WZ-I sample they vanish at 300^0C.

47
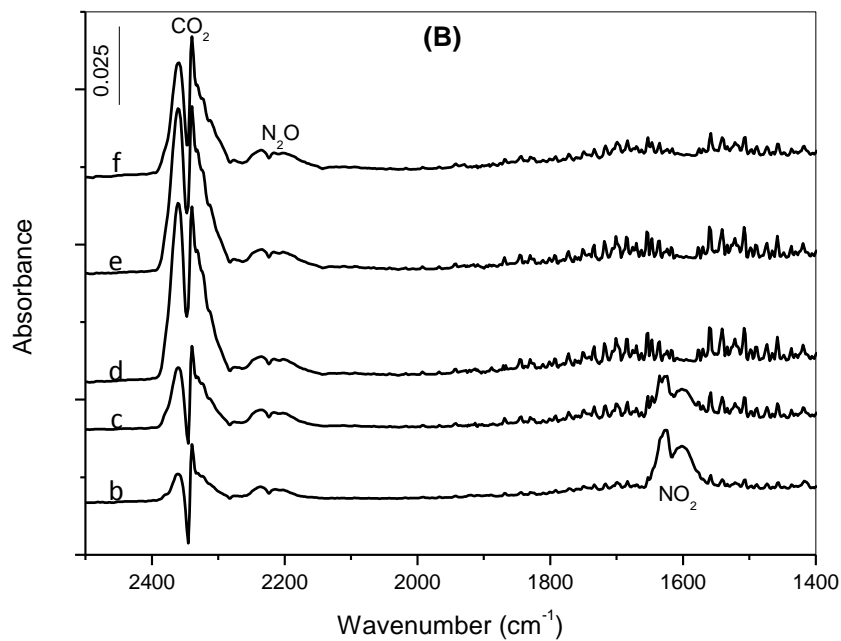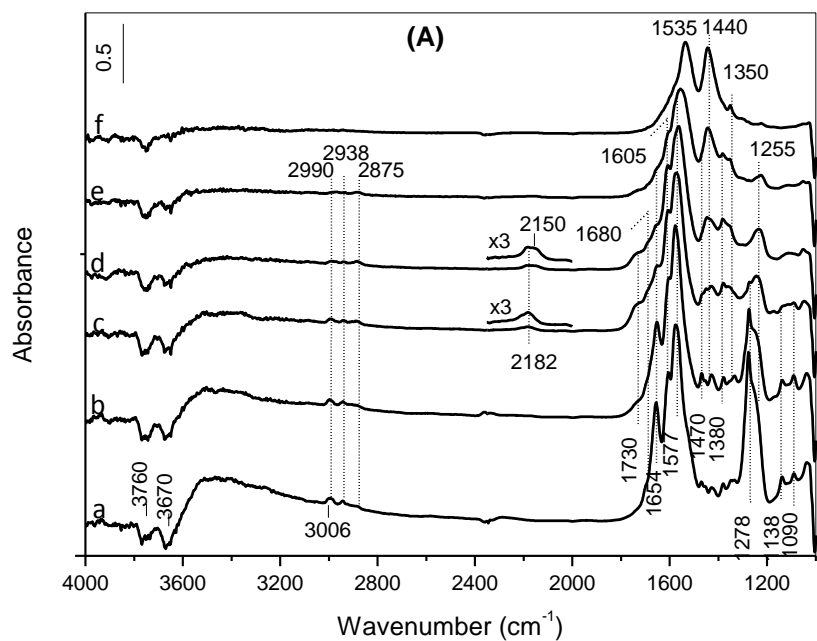
Fig. 20. Panel A: FT-IR spectra collected during the exposure of the Au/12WZ-I catalyst to a (10 Torr NO +3 Torr C_3H_6+25 Torr O_2) mixture at room temperature for 15 min followed by evacuation for 20 min (a) and heating the isolated IR cell for 15 min at 100^0C (b), 150^0C (c), 200^0C (d), 250^0C (e) and 300^oC (f),. Panel B: gas phase spectra at 100^0C (b), 150^0C (c), 200^0C (d), 250^0C (e) and 300^oC (f).

48
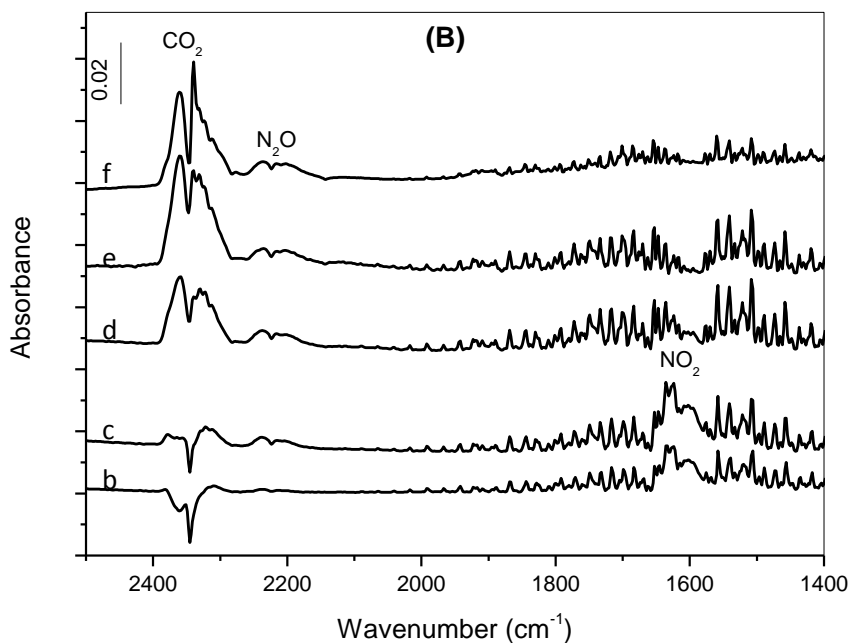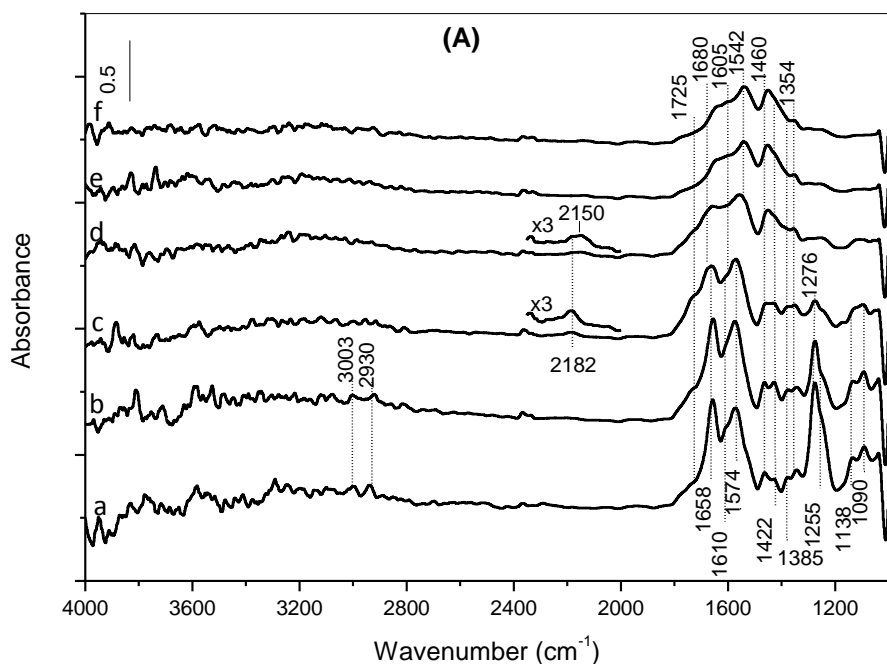
Fig. 21. Panel A: FT-IR spectra collected during the exposure of the Au/20WZ-I catalyst to a (10 Torr NO +3 Torr C_3H_6+25 Torr O_2) mixture at room temperature for 15 min followed by evacuation for 20 min (a) and heating the isolated IR cell for 15 min at 100^0C (b), 150^0C (c), 200^0C (d), 250^0C (e), 300^oC (f). Panel B: gas phase spectra at 100^0C (b), 150^0C (c), 200^0C (d), 250^0C (e), 300^oC (f).

49

Table 6. Assignment of the absorption bands observed during the investigation of the reactivity of surface species formed upon room-temperature adsorption of $NO+C_3H_6+O_2$ mixture on the Au/12WZ-I and Au/20WZ-I samples in the $25-250^0C$ temperature range.

Species	Band position, cm^{-1}	Vibration
C_3H_6 (ads)	3006-3003, 2990 2938-2930, 2875	$\nu(CH)$, $\nu_s(CH_2)$ $\nu_{as}(CH_3)$, $\nu_s(CH_3)$
Au^0-NCO (two types)	2182, 2150	$\nu_{as}(NCO)$
Isopropoxide (two types)	2938-2930, 2875 1138, 1090	$\nu_{as}(CH_3)$, $\nu_s(CH_3)$ $\nu(C-O)$
Acetone (ads)	2938-2930, 2875 1680	$\nu_{as}(CH_3)$, $\nu_s(CH_3)$ $\nu(C=O)$
Nitroacetone (ads)	2938-2930, 2875 1730-1725	$\nu_{as}(CH_3)$, $\nu_s(CH_3)$ $\nu(C=O)$
Bridged NO_3^- Bidentate NO_3^- (two types)	1658-1654, 1255 1610-1605, 1574 1278-1276	$\nu(N=O)$, $\nu_{as}(NO_2)$ $\nu(N=O)$ $\nu_{as}(NO_2)$
CH_3COO^- (two types)	1470-1460, 1440-1422 1385-1380, 1354-1350	$\nu_s(COO)$ $\delta(CH_3)$

These differences suggest that the best candidate for catalyst for the C_3H_6-SCR of NO_x could be the Au/20WZ-I sample. However, the catalyst efficiency for NO_x reduction should depend on the productivity of NCO species. The amount of NCO species produced on gold catalysts based on tungstated zirconia could be influenced at least by two factors: the gold dispersion and the ability of the catalyst to generate nitroacetone. Fig. 22 compares the

50

intensities of the Au–NCO bands detected at 200^0C during the $NO_x+C_3H_6$ surface reaction over all gold catalysts supported on tungstated zirconia. The complex absorption between 2200 and 2100 cm^{-1} reflects the presence of non-uniformity in the size of gold crystallites which affects the spectral features of the Au–NCO species. As explained above, the increase in the W content increases the gold uptake but at the same time causes decrease in the gold dispersion. The spectra in Fig. 22 clearly show that the amount of Au–NCO species formed is the highest on the Au/12WZ-I catalyst. This sample combines better gold dispersion with sufficient amount of Brønsted acid sites necessary for the activation of propene to hydrocarbon oxygenates leading to the formation of nitroacetone. It is concluded that among the materials studied, the zirconia-based catalyst containing 1.8 wt % gold and 12 wt % WO_3 (Au/12WZ-I) could be promising in the C_3H_6-SCR of NO_x.
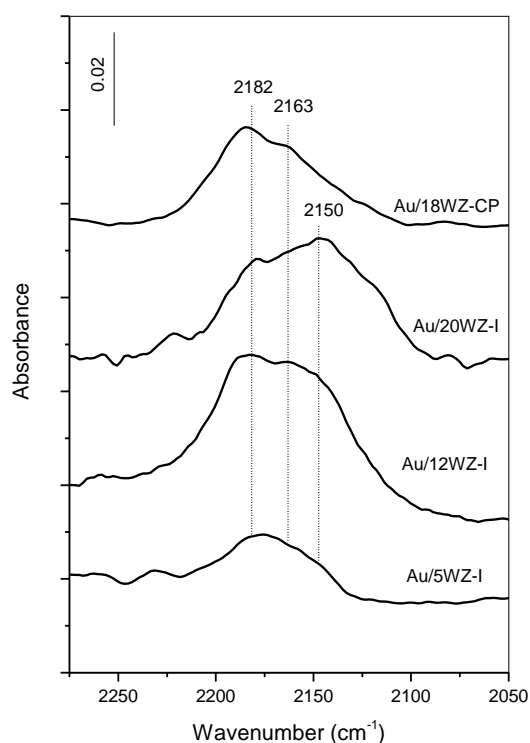

Fig. 22. FT-IR spectra collected during the exposure of the samples to a (10 Torr NO +3 Torr C_3H_6+25 Torr O_2) mixture at room temperature for 15 min followed by evacuation for 20 min and heating the isolated IR cell for 15 min at 200^0C.

Fig. 23 shows the development of the FT-IR spectra of the Au/12WZ-I and 12WZ-I samples in the 2300 – 1000 cm^{-1} region obtained in the presence of a gaseous mixture of 10 Torr NO + 3 Torr C_3H_6 + 25 Torr O_2 upon heating for 10 min at various temperatures. For both samples the predominant species observed at 100^{0}C are the bridged nitrates at 1651 and 1275 cm^{-1}, and bidentate nitrates at 1605, 1577-1573 and 1236 cm^{-1}. The signals at 1138 and 1090 cm^{-1} reveal the presence of isopropoxide species, whereas the band at 1735 – 1730 cm^{-1} belongs to adsorbed nitroacetone. The weak absorptions between 1500 and 1300 cm^{-1} correspond to different vibrational modes of the oxygenated derivatives of propene. At 150^{0}C the amount of adsorbed nitroacetone increases significantly which is accompanied by lowering of the concentration the surface nitrates and isopropoxides. The absorption at 1680 cm^{-1} clearly shows the formation of acetone as well. In the case of the Au-containing sample (Fig. 23A) weak unresolved absorption is detected at 2202 and 2175 cm^{-1}. The latter component corresponds to the ν_{as}(NCO) mode of NCO species coordinated to the gold particles [126,142,143]. The position of the Au–NCO band at lower wavenumber (2175 cm^{-1}) as compared with that in Fig. 20 (2182 cm^{-1}) can be associated with the increased concentration of the NCO species produced in the presence of C_3H_6+NO+O_2 gas mixture. The maximum at 2202 cm^{-1} (Fig. 22A) is attributed to NCO species adsorbed on the support. Most likely the corresponding isocyanates are attached to coordinatively unsaturated Zr^{4+} ions. This assignment is supported by the fact that the ν_{as}(NCO) stretching vibration of the complex ion $[Zr(NCO)_6]^{2-}$ is found at 2205 cm^{-1} [165].

The concentration of the NCO species on the surface of the Au/12WZ-I sample reaches maximum at 250^{0}C. This is accompanied by disappearance of the adsorbed nitroacetone (1730 cm^{-1}) and acetone (1680 cm^{-1}) and increase in the amount of the surface acetates with bands at 1555, 1534, 1450, 1425, 1380 and 1345 cm^{-1} (Fig. 23A). The NCO species disappear at 350^{0}C. This indicates that the isocyanates react with the NO_3^- species or activated NO_2 leading to disappearance of the surface nitrates.
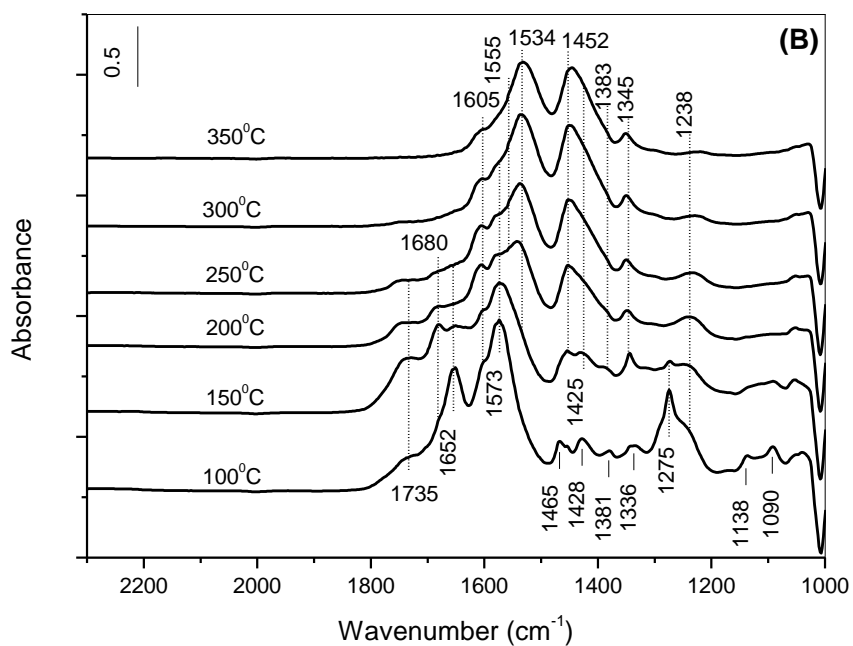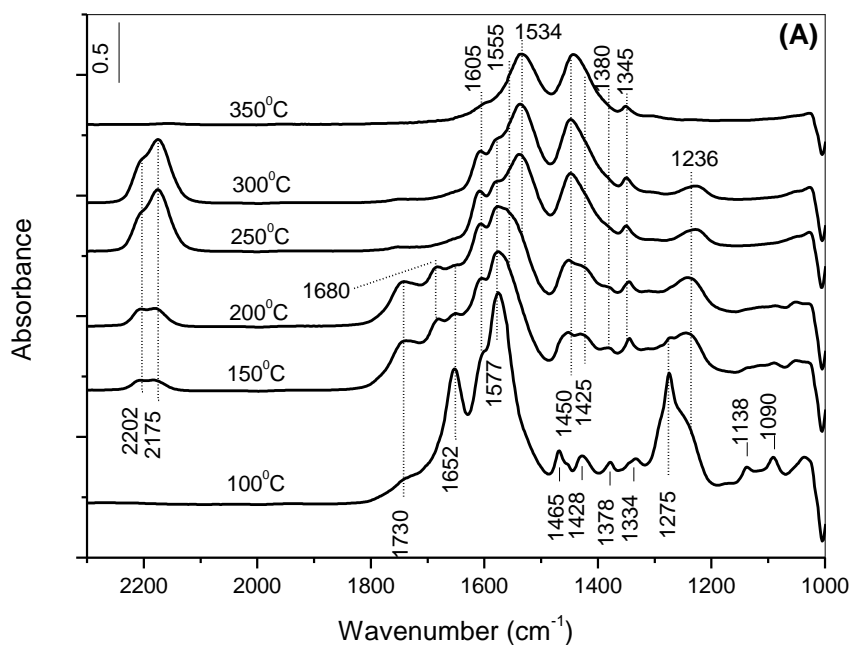
Fig. 23. FT-IR spectra of the Au/12WZ-I (Panel A) and 12WZ-I (Panel B) samples in the 2300 – 1000 cm^{-1} region obtained in the presence of a gaseous mixture of 10 Torr NO + 3 Torr C_3H_6 + 25 Torr O_2 and upon heating for 10 min at various temperatures.

In contrast to the Au/12WZ-I sample, at 250^0C nitroacetone and acetone are present on the surface of the support 12WZ-I (Fig. 23B). They disappear at 300^0C as a result of their further oxidation to acetates (bands at 1555, 1534, 1452, 1425, 1383 and 1345 cm^{-1}). Formation of NCO species is not detected in the $100 - 350^0$C temperature range and surface nitrates at 1605 and 1238 cm^{-1} are observed at 350^0C. This experimental fact suggests that the Au particles play fundamental role in the formation of the NCO species as proposed by reaction (1) and once formed on the metal particles they migrate on the support. In the case of the support (12WZ-I sample), the surface nitrates, respectively activated NO_2, are involved only in the formation of nitroacetone and acetone. The nitroketone undergoes thermal transformation to acetates and NO_x species at 200^0C and above, while the acetone is oxidized to acetates. This allows to conclude that the 12WZ-I sample does not catalyze the SCR of NO_x with propene.

3.5.3.4. Adsorption of acetone and its interaction with NO_2 over the Au/12WZ-I catalyst

The experimental results show that nitroacetone appears to be the key intermediate being the precursor of the NCO species. In order to confirm the assignment of the absorption band at 1730- 1735 cm^{-1} to adsorbed nitroacetone, we studied the adsorption of acetone and its interaction with NO_2 at various temperatures.

The adsorption of 12.8 Torr of acetone on the Au/12WZ-I sample at room temperature followed by evacuation for 10 min, produced the spectrum (a) in Fig. 24. The band at 1690 cm^{-1} is characteristic of the ν(C=O) stretching vibration of acetone coordinated to a Lewis acid site [29,30,156-158]. The intensities of the bands at 1420, 1368, 1242 and 1170 cm^{-1} decrease with the temperature simultaneously with the absorption at 1690 cm^{-1}. Based on this behavior, all these bands are attributed to various vibrational modes of adsorbed acetone (see Table 7). The bands at 1598 and 1443 cm^{-1} correspond to the ν_{as}(COO) and ν_s(COO) modes of acetate species, respectively. This experimental fact indicates that the Au/12WZ-I catalyst is able to oxidize the adsorbed acetone already at room temperature. Heating the isolated IR cell between 100 and 250^0C for 10 min at each temperature (Fig. 24, spectra (b) to (e)) leads to increase in the amount of the acetates (absorption bands at 1598, 1540, 1443, 1420, 1387 and 1315 cm^{-1}) at the expense of adsorbed acetone. The acetone disappears completely at 350^0C (spectrum (g)). The latter heat treatment does not lead to complete removal of the

acetates. Most likely the acetates are further oxidized to carbonates, which explains the enhancement of the intensity of the band at 1443 cm^{-1} observed at 350^{0}C. The assignment of the absorption bands is summarized in Table 7.
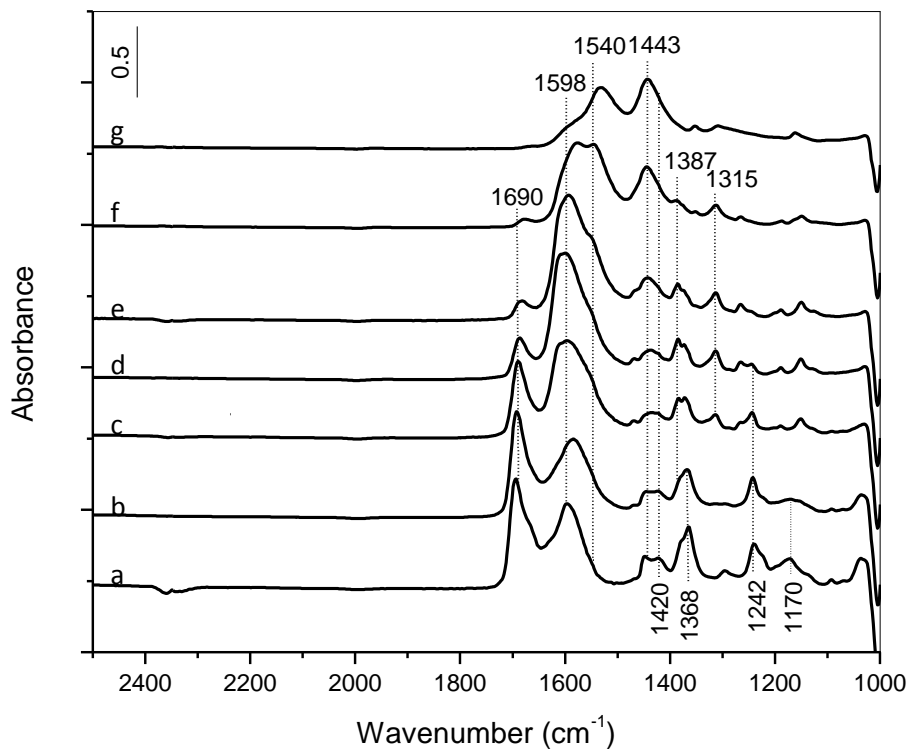

Fig. 24. FT-IR spectra of acetone (12.8 Torr) adsorbed on the Au/12WZ-I sample for 10 min at room temperature followed by evacuation for 10 min (a) and after heating the isolated IR cell for 10 min at 100^{0}C (b), 150^{0}C (c), 200^{0}C (d), 250^{0}C (e), 300^{0}C (f), and 350^{0}C (g).

Table 7. Assignments of the absorption bands in the spectra observed during the high-temperature adsorption of acetone and its coadsorption with NO_2 on the Au/12WZ-I catalyst.

Species	Band position, cm^{-1}	Vibration
Acetone (ads)	1690-1685	$\nu(C=O)$
	1420-1417	$\delta_{as}(CH_3)$
	1370-1368	$\delta_s(CH_3)$
	1242, 1170	$\nu_{as}(CCC), \nu_s(CCC)$
Nitroacetone (ads)	1732	$\nu(C=O)$
	1370	$\nu_s(NO_2)$
Bidentate NO_3^-	1605, 1245	$\nu(N=O), \nu_{as}(NO_2)$
(two types)	1575, 1275	$\nu(N=O), \nu_{as}(NO_2)$
CH_3COO^-	1598-1595, 1540-1535	$\nu_{as}(COO)$
(two types)	1444-1443, 1420	$\nu_s(COO)$
	1387-1385, 1350-1315	$\delta(CH_3)$
NCO	2205, 2180, 2165	$\nu_{as}(NCO)$
(three types of adsorption sites)		

The spectra shown in Fig. 25A are obtained during the interaction of NO_2 in the 25 – 350^{0}C temperature range with acetone adsorbed at room temperature on the surface of the Au/12WZ-I sample. The activated sample was left in contact with 12.8 Torr of acetone for 10 min at room temperature followed by evacuation for 10 min. Then to the IR cell 2 Torr of NO_2 were added and the isolated IR cell containing gaseous NO_2 was heated between 25 and 350^{0}C for 10 min at each temperature. The spectrum detected at room temperature (Fig. 25A, spectrum (a)) contains bands at 1685 ($\nu(C=O)$), 1420 ($\delta_{as}(CH_3)$) and 1370 cm^{-1} ($\delta_s(CH_3)$) of adsorbed acetone. The weak absorption at 1444 cm^{-1} suggests formation of acetate species and is attributed to the $\nu_s(COO)$ mode. The bands at 1605 and 1245 cm^{-1}, and at 1575 and

1275 cm^{-1} are due mainly to two types of bidentate nitrate species (ν(N=O) and ν_{as}(NO$_2$)

modes). The increase in the temperature to 100^{0}C (Fig. 25A, spectrum (b)) causes decrease in

the amounts of adsorbed acetone and nitrate species which is evident by lowering of the

intensities of the bands at 1685 and 1275 – 1245 cm^{-1}. At 150^{0}C (Fig. 25A, spectrum (c)) a

new band at 1732 cm^{-1} and a weak signal at 2180 cm^{-1} are detected. The gas phase spectrum

taken at 150^{0}C (Fig. 25B, spectrum (c)) shows that there is a decrease in the concentration of

gaseous NO$_2$. It can be concluded that the interaction between the acetone and nitrates species

(or activated NO$_2$) leads to the formation of the compound giving rise to the absorption at

1732 cm^{-1}. This feature is best assigned to the ν(C=O) mode of nitroacetone. The proposed

assignment is in agreement with the fact that nitroketones exhibit absorptions at 1730, 1560

and 1380 cm^{-1} corresponding to the ν(C=O), ν_{as}(NO$_2$) and ν_s(NO$_2$) modes [166]. The

antisymmetric NO$_2$ stretching vibration of nitroacetone is covered by the nitrate band at 1575

cm^{-1} and cannot be resolved. Another argument supporting the assignment of the absorption

at 1732 cm^{-1} to nitroacetone is the absence of this signal in the spectra of acetone adsorbed

alone (Fig. 24). At 200^{0}C (Fig. 25A, spectrum (d)) the intensity of the band at 2180 cm^{-1}

increases simultaneously with the appearance of a shoulder at 2205 cm^{-1}. These absorptions

were assigned to NCO species coordinated to gold particles and cationic sites of the support.

The appearance of the surface isocyanates parallels the formation of nitroacetone and

confirms the suggestion made above that they are formed through the transformation of

nitroketone. The sample and gas phase spectra taken at 200^{0}C (Fig. 25, spectra (d)) show also

that the concentrations of the nitrate species, respectively gaseous NO$_2$, have decreased

significantly. This fact allows to conclude that the NCO species react with the surface nitrates

and/or NO$_2$ to dinitrogen. Small amount of N$_2$O is formed as well (Fig. 25B). The surface

concentration of acetone decreases with the temperature as a result of its transformation to

nitroacetone. This process is dominant at 150^{0}C (Fig. 25A, spectrum (c)). At 200^{0}C the

acetone is oxidized mainly to acetate species which is evident by the increase in intensity of

the bands at 1444 and 1420 cm^{-1} corresponding to the ν_s(COO) modes of two types of

CH$_3$COO$^-$ species with ν_{as}(COO) stretching vibration located at ~1535 cm^{-1}. At 250^{0}C (Fig.

25A, spectrum (e)) the NCO species disappear simultaneously with the surface nitrates. Weak

absorption is detected at 2165 cm^{-1} which was attributed to less reactive NCO species

coordinated to larger gold particles (see Fig. 22). The acetone and its nitro derivative are no

longer present in the spectrum and the gaseous NO$_2$ is almost completely consumed (Fig.

25B, spectrum (e)). The surface acetates are thermally stable and they practically do not

undergo decomposition at 300 and 350^{0}C. This is the reason for the absence of CO_2 in the gas phase. Table 7 shows the assignment of the absorptions bands in the spectra detected during the adsorption of acetone and its coadsorption with NO_2 on the Au/12WZ-I sample.
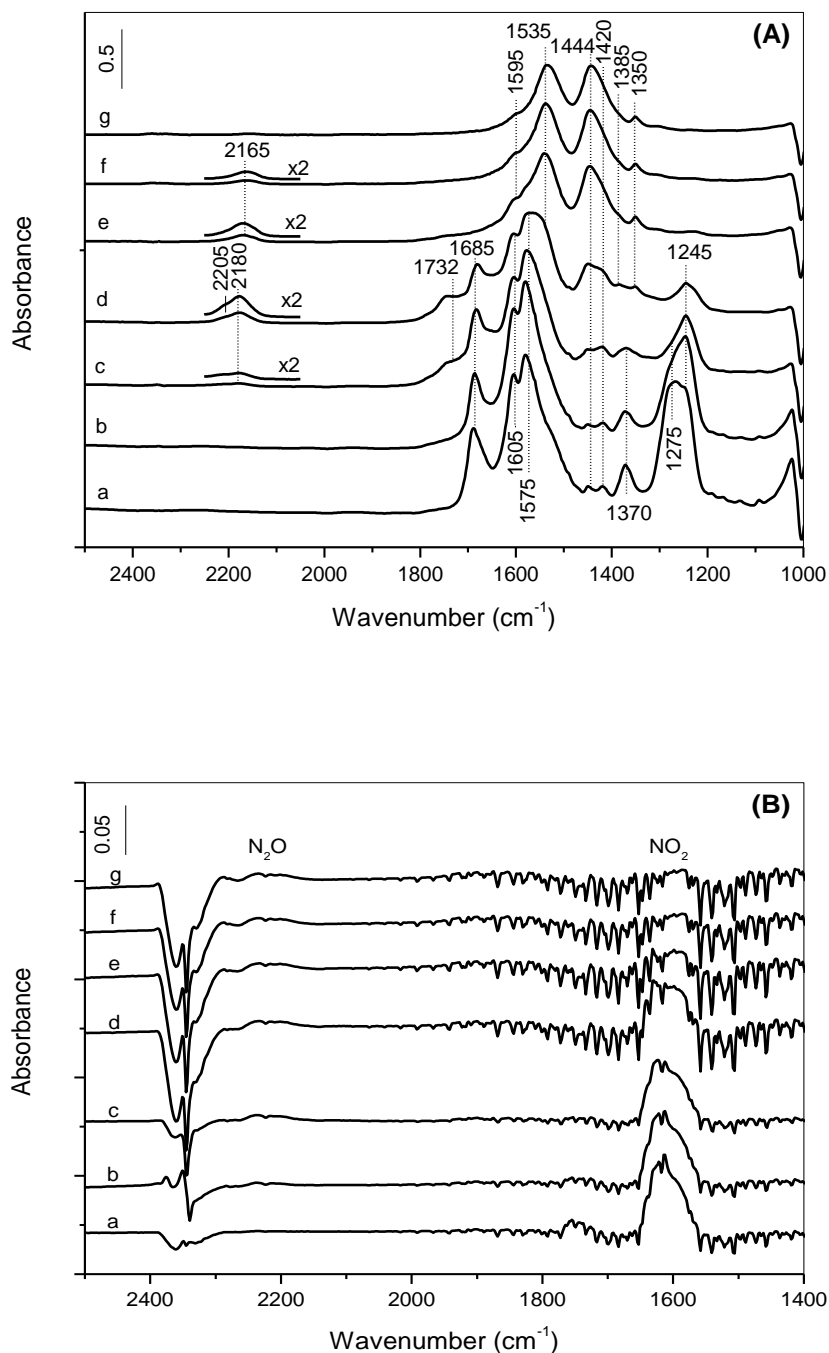

Fig. 25. FT-IR spectra of adsorbed acetone (12.8 Torr) on the Au/12WZ-I catalyst for 10 min at room temperature followed by evacuation for 10 min and addition of 2 Torr NO_2 (a) and after heating the isolated IR cell for 10 min at 100^{0}C (b), 150^{0}C (c), 200^{0}C (d), 250^{0}C (e), 300^{0}C (f), and 350^{0}C (g). Panel A is sample and panel B is gas phase.

The obtained results represent strong evidence that the nitroacetone and its transformation product, the NCO species, are the key intermediates in the SCR of NO_x by propene over the Au/12WZ-I catalyst.

3.6. Catalytic activity

Fig. 26 shows the NO reduction activity of Au/ZrO_2 and Au/12WZ-I catalysts at various temperatures. The NO conversion reaches 18% at 400^0C over the Au/ZrO_2 catalyst. The modification of zirconia by 12 wt % WO_3 increases the activity to 26% and lowers the temperature of maximum NO conversion by 50^0C. The analysis of the reaction products shows that the amounts of N_2O and NO_2 are negligible small, which indicates that the Au/12WZ-I catalyst is characterized by high selectivity. The obtained results are encouraging and we believe that the performance of gold catalysts based on tungstated zirconia could be improved by optimization of gold dispersion and catalyst composition.
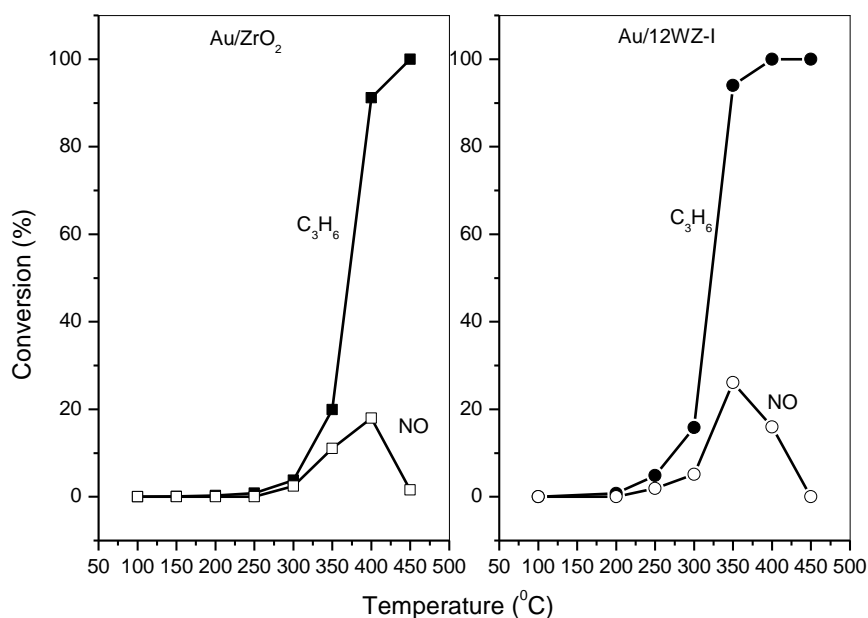

Fig. 26. Catalytic activity for NO reduction with propene over Au/ZrO_2 and Au/12WZ-I catalysts. Reagent gas mixture: 1400 ppm of propene, 300 ppm of NO, 4 vol. % of O_2 in He; WHSV = 30000 ml/g·h

59

4. CONCLUSIONS

Gold catalysts supported on tungstated zirconia (containing 5 – 20 wt % WO_3) can be prepared by cationic adsorption from aqueous solution of $[Au(en)_2]Cl_3$ complex. According to XRD and XPS data large (8 – 10 nm) and small (~ 3 nm) gold particles are present on the catalyst surfaces.

The FT-IR spectra of adsorbed CO show the formation of two types of Au−CO bands, at 2128 – 2135 cm^{-1} (high-frequency band) and 2113 – 2116 cm^{-1} (low-frequency band), which are attributed to CO coordinated to large and small gold particles, respectively. It is concluded that the gold particles occupy preferentially the WO_x-free zirconia surface and the dispersion of gold depends on the amount of coodinatively unsaturated (cus) Zr^{4+} ions. Modification of zirconia by WO_3 increases the gold uptake but at the same time causes decrease in the concentration of (cus) Zr^{4+} ions. Consequently, the fraction of large gold particles increases.

The interaction of Au/ZrO_2 and Au/ZrO_2-WO_x samples with $NO+O_2$ gas mixture shows that the W-containing samples promote the formation of NO_2 at room temperature. The amount of the surface nitrates produced during the $NO+O_2$ co-adsorption decreases with increase in the W loading due to lowering of the basicity of the surface O^{2-} ions. The major product of decomposition of the adsorbed NO_3^- species is NO_2.

Contrary to some reports in the literature, we have found that the treatment of gold supported on tungstated zirconia with $NO+O_2$ mixture at room temperature does not cause oxidation of the gold particles. However, the subsequent adsorption of CO on NO_x-precovered Au/ZrO_2-WO_x catalyst leads to the formation of NCO species coordinated to gold particles. The generation of NCO species at low temperature offers the possibility for development of low-temperature catalyst for selective reduction of NO_x with CO. The NCO species are considered to be reactive intermediates in this reaction.

The analysis of FT-IR spectra recorded during the oxidation of propene over the Au/ZrO_2 catalyst indicates that this sample catalyzes the deeper oxidation of the hydrocarbon. In the case of WO_x-containing gold catalysts, the amount of partially oxidized hydrocarbons produced during the $C_3H_6 + O_2$ reaction increases with increase in the tungsten content. This

result is in agreement with the fact that the presence of Brønsted acidity combined with redox sites such as W=O groups facilitate the partial oxidation of propene.

The results of detailed mechanistic investigation show that the activation of propene in the presence of NO_x species adsorbed on Au/ZrO_2-WO_x samples takes place at room temperature producing surface isopropoxides. The interaction of the latter species with the surface nitrate complexes leads to the formation of nitroacetone. It is proposed that at higher temperature (150^0C) the nitroacetone transforms through an internal redox process producing NCO species and surface acetates. The fact that no surface isocyanates are observed over Au-free ZrO_2-WO_x samples leads to the conclusion that this process is catalyzed by the gold nanoparticles. The NCO species react with the NO_3^-/NO_2 surface complex formed by oxidation of NO yielding molecular nitrogen, N_2O and CO_2 as reaction products.

The amount of NCO species produced on the gold catalysts supported on tungstated zirconia depends on the gold dispersion and it is the highest in the case of a catalyst containing 1,8 wt % Au and 12 wt % WO_3. The modification of zirconia by 12 wt % of WO_3 increases the activity of the gold catalyst in the reaction of selective NO reduction with propene and lowers the temperature of maximum NO conversion by 50^0C. The analysis of the reaction products shows that the amounts of N_2O and NO_2 are negligibly small, which indicates that the catalyst is characterized by high selectivity.

The obtained results are encouraging and confirm the hypothesis that gold supported on tungstated zirconia can act as a bifunctional catalyst in the selective reduction of NO by propene. The WO_x species facilitate the process of NO oxidation and ensure significant amount of oxygenated derivatives of the hydrocarbon (nitroacetone), whereas the gold particles play fundamental role in the conversion of nitroketone to NCO species, the reactive intermediates of the reaction.

5. REFERENCES

1. www.ipcc.ch

2. www.epa.gov

3. ec.europa.eu

4. M.D. Amiridis, T. Zhang, R.J. Farrauto, Appl. Catal. B, 10, (1996), 2

5. F. Klinstedt, K. Arve, K. Eranen, D. Yu. Murzin, Acc. Chem. Res, 39 (2006) 273.

6. R.M. Heck, R.J. Farrauto, Appl. Catal. A, 221 (2001) 443.

7. J. Kaspar, P. Fornasiero, N. Hickey, Catal. Today, 77 (2003) 419.

8. R. Burch, Catal. Rev. 46 (2004) 271.

9. J. M. Trichard, Stud. Surf. Sci. Catal., 171 (2007) 211.

10. L. J. Gill, Ph. G. Blakeman, M.V. Twigg, A. P. Walker. Topics Catal., 28 (2004) 157.

11. J. A. Sullivan, J. A. Doherty, Appl. Catal. B, 55 (2005) 185.

12. P. Forzatti, Appl. Catal. A, 222 (2001) 221.

13. M. Koebel, G. Madia, M. Elsener, Catal. Today, 73 (2002) 239.

14. W. Held, A. Koenig, T. Richter, L. Puppe, SAE paper, 1990, 900496, 13.

15. M. Iwamoto, H. Yahiro, S. Shundo, Y. Yu-u, N. Mizuno, Shokubai, 32 (1990) 430.

16. M. C. Kung, H. H. Kung, Top. Catal. 28 (2004) 105.

17. R. Burch, J. P. Breen, F.C. Meunier, Appl. Catal. B, 39 (2002) 283.

18. I. Cayirtepe, A. Naydenov, G. Ivanov, M. Kantcheva, Catal Lett., 438-449 (2009) 132.

19. R. Burch, J. P. Breen, C.J. Hill, B. Krutzsch, B. Konrad, E. Jobson, L. Cider, K. Eranen, F. Klingstedt, L.-E. Lindfors, Top. Catal., 30-31 (2004) 19.

20. A. Ueda, M. Haruta, Gold Bulletin 32 (1999) 3.

21. A. Ueda, T. Oshima, M. Haruta, Appl. Catal. B 12 (1997) 81.

22. A. Ueda, M. Haruta, Appl. Catal B 18 (1998) 115.

23. L. Q. Nguyen, C. Salim, H. Hinode, Top. Catal. 52 (2009) 779.

24. M. Misono, Y. Hirao, Ch. Yokoyama, Catal. Today 38 (1997) 157.

25. Ch. Yokoyama, M. Misono, Catal. Lett. 29 (1994) 1.

26. N. Le To Nga, Cl. Potvin, G. Djega-Mariadassou, L. Delannoy, C. Louis, Top. Catal. 42-43 (2007) 91.

27. B. Grzybowska-Swierkosz, Catal. Today 112 (2006) 3.

28. G. Busca, Phys. Chem. Chem. Phys. 1 (1999) 723.

29. V. Sanches Escibano, G. Busca, V. Lorenzelli, J. Phys. Chem. 94 (1990) 8939.

30. E. Finocchio, G. Busca, V. Lorenzelli, V. Sanches Escibano, J. Chem. Soc. Faraday Trans. 92 (1996) 1587.

31. M. Kantcheva, I. Cayirtepe, J.Mol. Catal. A, 247 (2006) 88.

32. G. R Bamwenda, A. Obuchi, A. Ogata, J. Oi, S. Kushiyama, K. Mizuno, J. Mol. Catal. A 126 (1997) 151.

33. R. Burch, P. J. Millington, A. P. Walker, Appl. Catal. B, 4 (1994) 65.

34. T. Chafik, S. Kameoka, Y. Ukisu and T. Miyadera, J. Mol. Catal. A 136 (1998) 203.

35. T. Tanaka, T. Okuhara and M. Misono, Appl. Catal. B, 4 (1994) L1.

36. T. Okuhara, Y. Hasada and M. Misono, Catal. Today, 35 (1997) 83.

37. K. A. Bethke, C. Li, M.C. Kung, B. Yang and H.H. Kung, Catal. Lett. 31 (1995) 287.

38. Y. Ukisu, S. Sato, A. Abe and K. Yoshida, Appl. Catal. B 2 (1993) 147.

39. B. Djonev, B. Tsyntsarski, D. Klissurski and K. Hadjiivanov, J. Chem. Soc., Faraday Trans. 93 (1997) 4055.

40. M. Yamaguchi, J. Chem. Soc., Faraday Trans. 93 (1997) 3581.

41. A.D. Cowan, N.W. Cant, B.S. Haynes and P.F. Nelson, J. Catal. 176 (1998) 329.

42. S. Kameoka, T. Chafik, Y. Ukisu and T. Miyadera, Catal. Lett. 51 (1998) 11.

43. M. Haneda, Y. Kintaichi, M. Inaba and H. Hamada, Catal. Today 42 (1998) 127.

44. F.C. Meunier, J.P. Breen, V. Zuzaniuk, M. Olsson and J.R.H. Ross, J. Catal. 187 (1999) 493.

45. V. Zuzaniuk, F.C. Meunier and J.R.H. Ross, J. Catal. 202 (2001) 340.

46. M. Haneda, E. Joubert, J.-C. Menezo, D. Duprez, J. Barbier, N. Bion, M. Daturi, J. Saussey, J.-C. Lavalley and H. Hamada, J. Mol. Catal. A 175 (2001) 179.

47. V. A. Sadykov, S.L. Baron, V.A. Matyshak, G.M. Alikina, R.V. Bunina, A.Y. Rozovskii, V.V. Lunin, E.V. Lunina, A.N. Kharlanov, A.S. Ivanova, S.A. Veniaminov, Catal. Lett. 37 (1996) 157.

48. V. A. Sadykov, V.V. Lunin, V.A. Matyshak, E. A. Paukshtis, A. Y. Rozovskii, N.N. Bulgakov, J. R. H. Ross, Kinet. Katal., 44 (2003) 379.

49. V.A. Matyshak, V. F. Tret'yakov, K. A. Chernishev, T. N. Burdeinaya, V. N. Korchak, V. A. Sadykov, Kinet. Katal., 47 (2006) 747.

50. O. Gorce, F. Baudin, C. Thomas, P. Da Costa, G. Djega-Mariadassou, Appl. Catal. B, 54 (2004) 69.

51. N. El Kolli, C. Potvin, C. Thomas, J. Catal., 259 (2008) 240.

52. M. Kantcheva, I. Cayirtepe, Catal. Lett., 115 (2007) 148.

53. M. Kantcheva, H. Budunoglu and O. Samarskaya, Catal. Commun., 9 (2008) 874.

54. G. R. Bamwenda, A. Obuchi, S. Kushiyama, K. Mozono, Stud. Surf. Sci. Catal 130 (2000) 1271.

55. K.-I. Shimizu, H. Kawabata, A. Satsuma and T. Hattori, J. Phys. Chem. B 103 (1999) 5240.

56. K.-I. Shimizu, J. Shibata, H. Yoshida, A. Satsuma and T. Hattori, Appl. Catal. B 30 (2001) 151.

57. J.-H. Lee, A. Yezerets, M.C. Kung and H.H. Kung, Chem. Commun. 15 (2001) 1404.

58. M. Kantcheva, J. Catal., 204 (2001) 479.

59. M. Kantcheva, Appl. Catal. B, 42 (2003).

60. H. Hamada, Y. Kintaichi, M. Sasaki and T. Ito, Appl. Catal. 75 (1991) L1.

61. H. Hamada, Y. Kintaichi, M. Sasaki, T. Ito and T. Yoshinari, Appl. Catal. A, 88 (1992) L1.

62. T. Miyadera, Appl. Catal. B 2 (1993) 199.

63. M. Tabata, H. Tsuchida, K. Miyamoto, T. Yoshinari, H. Yamazaki, H. Hamada, Y. Kintaichi, M. Sasaki and T. Ito, Appl. Catal. B 6 (1995) 169.

64. Y. Ukisu and T. Miyadera, Catal. Lett. 39 (1996) 265.

65. R. Burch, E. Halpin and J.A. Sullivan, Appl. Catal. B 17 (1998) 115.

66. T.J. Toops, A.B. Walters and M.A. Vannice, Catal. Lett. 64 (2000) 65.

67. J.G. Santiesteban, J. V. Vartuli, S. Han, R. D. Bastian, C. D. Chang, J. Catal. 168 (1997) 431.

68. A. Martinez, G. Prieto, M. A. Arribas, P. Concepcion, J. F. Sanchez-Royo, J. Catal. 248 (2007) 288.

69. B. P. Block, J. C. Bailar, Jr., J. Am. Chem. Soc. 73 (1951) 4722.

70. R. A. Boyse, E. Ko, J. Catal. 171 (1997) 191.

71. M. Scheithauer, R. K. Grasselli, H. Knozinger, Langmuir 14 (1998) 3019.

72. D. G. Barton, M. Shtein, R. D. Wilson, S. T. Soled, E. Iglesia, J. Phys. Chem B 103 (1999) 630.

73. E. I. Ross-Medgaarden, W. V. Knowles, T. Kim, M. S. Wong, W. Zhou, C. J. Kiely, I. E. Wachs, J. Catal. 256 (2008) 108.

74. M. Kantcheva, C. Koz, J. Mater. Sci. 42 (2007) 6074.

75. E. I. Ross-Medgaarden, I. E. Wachs, J. Phys. Chem. C 111 (2007) 15089.

76. F. Di Gregorio, V. Keller, J. Catal. 225 (204) 45.

77. V. Bolis, G. Cerrato, G. Magnaca, C. Morterra, Thermochim. Acta 312 (1998) 63.

78. K. T. Jung, A. T. Bell, J. Mol. Catal. A 163 (2000) 27.

79. J. Li, J. Chen, W. Song, J. Liu, W. Shen, Appl. Catal. A 334 (2008) 321.

80. C. E. Crouthamel, C. E. Johnson, Anal. Chem. 26 (1954) 1284.

81. D. F. Wood, R. T. Clark, Analyst 83 (1958) 326.

82. F. P. J. M. Kerkhof, J. A. Moulijn, J. Phys. Chem. 83 (1979) 1612.

83. V. Leon, Surf. Sci. 339 (1995) L931.

84. M. Haruta, Catal. Surv. Japan 1 (1997) 61.

85. M. Haruta, Gold Bulletin 37 (2004) 27.

86. G. C. Bond, D. T. Thompson, Catal. Rev.-Sci. Eng. 41 (1999) 319.

87. M. C. Kung, J.-H. Lee, Chu Kung, H.H. Kung, Stud. Surf. Sci. Catal. 101 (1996) 701.

88. M. C. Kung, K. A. Bethke, J. Yan, J.-H. Lee, H.H. Kung, Appl. Surf. Sci. 121/122 (1997) 261.

89. E. Seker, E. Gulari, Appl. Catal. A 232 (2002) 203.

90. G. Hutchings, Catal. Today 100 (2005) 55.

91. E. D. Park, J. S. Lee, J. Catal. 186 (1999) 1.

92. A. P. Kozlova, A. I. Kozlov, S. Sugiyama, Y. Matsui, K. Asakura, Y. Iwasawa, J. Catal. 181 (1999) 37.

93. M. Kosmulski, J. Colloid Interface Sci. 253 (2002) 77.

94. S. Ivanova, C. Petit, V. Pitchin, Appl. Catal. A 267 (2004) 191.

95. P. Mukherjee, C. R. Patra, A. Ghosh, R. Kumar, M. Sastry, Chem. Mater. 14 (2002) 1678.

96. D. Guillemot, M. Polisset-Thfoin, J. Fraissard, Catal. Lett. 41 (1996) 143.

97. D. Guillemot, V. Yu. Borovkov, V. B. Kazansky, M. Polisset-Thfoin, J. Fraissard, J. Chem. Soc. Faraday Trans. 93 (1997) 3587.

98. R. Zanella, A. Sandoval, P. Santiago, V. A. Basink, J. M. Saniger, J. Phys. Chem. B 110 (2006) 8559.

99. H. Zhu, C. Liang, W. Yan, S. H. Overbury, S. Dai, J. Phys. Chem. B 110 (2006) 10842.

100. H. Zhu, Zh. Ma, J. C. Clark, Zh. Pan, St. H. Overbury, Sh. Dai, Appl. Catal A 326 (2007) 89.

101. A. A. Isab, M. N. Shaikh, M. Monim-ul-Mehbood, B. A. Al-Maythalony, M. I. M. Wazeer, S. Altuwaijri, Spectrochim. Acta A, 79 (2011) 1196.

102. B. A. Al- Maythalony, M. I. M. Wazeer, A. A. Isab, Inorg. Chim. Acta 362 (2009) 3109.

103. E. V. Makotchenko, Russ. J. Coord. Chem. 29 (2003) 778.

104. E. V. Makotchenko, V. I. Malkova, Russ. J. Coord. Chem. 31 (2005) 703.

105. M. A. Cortes-Jacome, C. Angeles-Chavez, E. Lopez-Salinas, J. Navarrete, P. Toribo, J. A. Toledo, Appl. Catal. A 318 (2007) 178.

106. F. Boccuzzi, G. Cerrato, F. Pinna, G. Strukul, J. Phys. Chem B 102 (1998) 5733.

107. R. Kydd, J. Scott, W. Y. Teoh, K. Chiang, R. Amal, Langmiur 26 (2010) 2099.

108. S. Eustis, M. A. El-Sayed, Chem. Soc. Rev. 35 (2006) 209.

109. X. Zhang, H. Wang, Bo-Q. Xu, J. Phys. Chem B 109 (2005) 9678.

110. Y. Azizi, C. Petit, V. Pitchon, J. Catal. 269 (2010) 26.

111. S. Schimpf, M. Lucas, C. Mohr, U. Rodemerck, A. Bruckner, J. Radnik, H. Hofmeister, P. Claus, Catal. Today 72 (2002) 63.

112. L. Ilieva, J. W. Sobczak, M. Manzoli, B. L. Su, D. Andreeva, Appl. Catal. A 291 (2005) 85.

113. R. Zanella, L. Dellanoy, C. Louis, Appl. Catal. A 291 (2005) 62.

114. R. Wojcieszak, M. J. Genet, P. Eloy, P. Ruiz, E. M. Gaigneaux, J. Phys. Chem. 114 (2010) 16677.

115. S. Velu, K. Suzuki, Chinnakonda S. Gopinath, H. Yoshidac, T. Hattori, Phys. Chem. Chem. Phys. 4 (2002) 1990.

116. L.-C. Wang, Q. Liu, M. Chen, Y.-M. Liu, Y. Cao, He-Y. He, K.-N. Fan, J. Phys. Chem. C 111 (2007) 16549.

117. R. Grabowski, J. Sloczynski, M. Sliwa, D. Mucha, R. P. Socha, ACS Catal. 1 (2011) 266.

118. J.C. Dupin, D. Gonbeau, P. Vinatier, A. Levasseur, Phys. Chem. Chem. Phys. 2 (2000) 1319.

119. J.-D. Grunwald, M. Macviejewski, O. S. Becker, P. F. Fabrizioli, A. Baiker, J. Catal. 186 (1999) 458.

120. M. Maciejewski, P. Fabrizioli, J.-D. Grunwald, O. S. Becker, A. Baiker, Phys. Chem. Chem. Phys. 3 (2001) 3846.

121. M. Manzoli, A. Chiorino, F. Boccuzzi, Surf. Sci. 532-535 (2003) 377.

122. M. Kantcheva, E. Z. Ciftlikli, J. Phys. Chem. B 106 (2002) 3941.

123. C. Morterra, G. Cerrato, V. Bolis, C. Lamberti, L. Ferroni, L. Montanaro, J. Chem. Soc. Faraday Trans. 91 (1995) 113.

124. F. Boccuzzi, A. Chiorino, J. Phys. Chem. B 104 (2000) 5414.

125. K. I. Hadjiivanov, G. N. Vayssilov, Adv. Catal. 47 (2002) 307.

126. M. Kantcheva, O. Samarskaya, L. Ilieva, G. Pantaleo, A. M. Venezia, D. Andreeva, Appl. Catal. B 88 (2009) 113.

127. D. Andreeva, M. Kantcheva, I. Ivanov, L. Ilieva, J. W. Sobczak, W. Lisowski, Catal. Today 158 (2010) 69.

128. F. Vindigni, M. Manzolli, A. Chiorino, F. Boccuzzi, Gold Bull. 42 (2009) 106.

129. M. A. Centeno, K. Hadjiivanov, T. Venkov, H. Klimev, J. A. Odriozola, J. Mol. Catal. A: Chem. 252 (2006) 142.

130. M. Mihaylov, B. C. Gates, J. F. Fierro-Gonzales, K. Hadjiivanov, H. Knözinger, J. Phys. Chem. C 111 (2007) 2548.

131. K. Musialska, E. Finocchio, I, Sobczak, G. Busca, R. Wojcieszak, E. Gaigneaux, M. Ziolek, Appl. Catal. A 384 (2010) 70.

132. M. S. Chen, D. W. Goodman, Science 306 (2004) 252.

133. M.M. Kantcheva, V.P. Bushev, K.I. Hadjiivanov, J. Chem. Soc., Faraday Trans. 88 (1992) 3087.

134. K. Hadjiivanov, V. Bushev, M. Kantcheva, D. Klissurski, Langmuir 10 (1994) 464.

135. M. Kantcheva, A.S. Vakkasoglu, J. Catal. 223 (2004) 364.

136. B. Tsyntsarski, V. Avreyska, H. Kolev, T. Marinova, D. Klissurski, K. Hadjiivanov, J. Mol. Catal. A: Chem. 193 (2003) 139.

137. T. Weingand, S. Kuba, K. Hadjiivanov and H. Knözinger, J. Catal. 209 (2002) 539.

138. Tz. Venkov, K. Fajerwerg, L. Delannoy, Hr. Klimev, K. Hadjiivanov, C. Louis, Appl. Catal. A 301 (2006) 106.

139. S. Minico, S. Scire, C. Crisafulli, A. M. Visco, S. Galvagno, Catal. Lett. 47 (1997) 273.

140. M. Li, Z. Wu, Z. Ma, V. Schwartz, D. R. Mullins, S. Dai, S. H. Overbury, J. Catal. 266 (2009) 98.

141. M. A. Dekkers, M. J. Lippits, B. N. Nieuwenhuys, Catal. Lett. 56 (1998) 195.

142. F. Solymosi, T. Bansagi, T. Suli Zakar, Phys. Chem. Chem. Phys. 5 (2003) 4724.

143. F. Solymosi, T. Bansagi, T. Suli Zakar, Catal. Lett. 87 (2003) 7.

144. H. Celio, K. Mudalige, P. Mills, M. Trenary, Surf. Sci. 394 (1997) L168.

145. T. Nanba, K.-ichi Wada, S. Masukawa, J. Uchisawa, A. Obuchi, Appl. Catal. A 380 (2010) 66.

146. G. Piazzesi, O. Kröcher, M. Elsener, A. Wokaun, Appl. Catal. B 65 (2006) 55.

147. F. Solymosi and T. Bánsági, J. Phys. Chem. 83 (1979) 552.

148. C. Li, K. A. Bethke, H. H. Kung and M. C. Kung, J. Chem. Soc. – Chem. Commun. (1995) 813.

149. S. Sumiya, H. He, A. Abe, N. Takezawa and K. Yoshida, J. Chem. Soc. Faraday Trans. 94 (1998) 2217.

150. K. Shimizu, H. Kawabata, H. Maeshima, A. Satsuma and T. Hattori, J. Phys. Chem. B 104 (2000) 2885.

151. Y. Chi and S. S. C. Chuang, J. Catal. 190 (2000) 75.

152. Y. Jugnet, F. J. Cadete Santos Aires, C. Deranlot, L. Piccolo, J. C. Bertolini, Surf. Sci. 521 (2002) L639

153. G. Busca, G. Ramis, V. Lorenzelli, A. Janin and J. C. Lavalley, Spectrochim. Acta 43A (1987) 489.

154. B. Bachiller-Baeza, I. Rodriguez-Ramos, A. Guerrero-Ruiz, Langmuir 14 (1998) 3556.

155. K. Pokrovski, K. T. Jung, A. T. Bell, Langmuir 17 (2001) 4297.

156. E. Finocchio, R. J. Willey, G. Busca and V. Lorenzelli, J. Chem. Soc. Faraday Trans. 93 (1997) 175.

157. G. Busca, E. Finocchio, V. Lorenzelli, G. Ramis and M. Baldi, Catal. Today 49 (1999) 453.

158. M. A. Hasan, M. I. Zaki and L. Pasupulety, Appl. Catal. A 243 (2003) 81.

159. P. F. Rossi, G. Busca, V. Lorenzelli, O. Saur and J. C. Lavalley, Langmuir 3, (1987) 52.

160. Y. Toda, T. Ohno, F. Hatayama and H. Miyata, Phys. Chem. Chem. Phys. 1 (1999) 1615.

161. M. I. Zaki, M. A. Hasan and L. Pasupulety, Langmuir 17 (2001) 4025.

162. S. Alessandrini , I. Collamati and C. Ercolani J. Chem. Soc., Dalton Trans., 1973, 2409.

163. Y. Ukisu, S. Sato, G. Muramatsu and K. Yoshida, Catal. Lett. 16 (1992) 11.

164. A. Satsuma, A. D. Cowan, N. W. Cant and D. L. Trimm, J. Catal. 181 (1999) 165.

165. K. Nakomoto, *Infrared and Raman Spectra of Inorganic and Coordination Compounds Part B,* 6th ed. p. 127 New Jersey; Wiley (2009).

166. L. L Adams, F. A. Luzzio, J. Org. Chem. 54 (1989) 5387.

Some parts of this thesis are in press as:

1. *M. Kantcheva, M. Milanova, I. Avramova, S. Mametsheripov, Spectroscopic characterization of gold supported on tungstated zirconia, Catal. Today (2012), doi:10.1016/j.cattod.2012.02.027*

2. *M. Kantcheva, M. Milanova, S. Mametsheripov, In situ FT-IR spectroscopic investigation of gold supported on tungstated zirconia as catalyst for CO-SCR of NOx, Catal. Today (2012), http://dx.doi.org/10.1016/j.cattod.2012.03.058*